Chemical Engineering Journal 543 (2026) 178604

Contents lists available at ScienceDirect

Chemical Engineering Journal

journal homepage: www.elsevier.com/locate/cej

Thioctic acid–functionalized silica for selective palladium adsorption from chloride–based solutions

Amir Nobahar [a,*], Flavia N. Braga [a,b], Rita M. Carvalho [b,c], Helena Passos [b], Filipe H.B. Sosa [a], Nicolas Schaeffer [a,*], João A.P. Coutinho [a]

[a] CICECO–Aveiro Institute of Materials, Department of Chemistry, University of Aveiro, 3810–193, Aveiro, Portugal
[b] LSRE–LCM, ALiCE, Faculty of Engineering, University of Porto, Rua Dr. Roberto Frias, 4200–465, Porto, Portugal
[c] RYA – Purification Technologies, PCI – Creative Science Park, 3830–352, Ílhavo, Portugal

ARTICLE INFO

Keywords:
Platinum group metals
Hydrometallurgical separation
Sulfur–functionalized silica
Selective adsorption
Disulfide ligands

ABSTRACT

Selective recovery of Pd from chloride-rich hydrometallurgical leachates, such as those derived from automotive catalytic converters, remains challenging due to the chemical similarity of PGMs and the stability of their chloro-complexes. Here, we report a green, selective sorbent (TA@Si) prepared by covalently grafting the naturally occurring disulfide ligand, thioctic acid, onto mesoporous silica via silane chemistry. In multi-metal batch experiments, TA@Si exhibited excellent selectivity for Pd over Pt, Rh, and base metals (Fe, Zn, Ce) across a wide acidity range (0.05–10 M HCl). The process was endothermic and entropy-driven, remaining thermodynamically favorable under strongly acidic conditions, and adsorption followed pseudo-second-order kinetics, best described by Sips and Temkin isotherm models, reaching a maximum capacity of (49.5 ± 12.4) $mg{\cdot}g^{-1}$ at 0.2 M HCl. XPS, Raman spectroscopy and SEM-EDS analyses indicate that Pd(II) coordinates to disulfide-derived sulfur sites of TA, forming stable surface-anchored Pd-S/Cl complexes. Adsorbed Pd (along with minor Pt) was quantitatively recovered using thiourea in dilute HCl, and the sorbent maintained performance over at least five adsorption-desorption cycles. Fixed-bed column studies demonstrated that this selectivity translates to continuous operation, with delayed Pd breakthrough, minimal co-adsorption of competing metals, and efficient Pd recovery through continuous thiourea-assisted desorption.

This work introduces an acid-stable thioctic-acid-functionalized silica adsorbent for selective Pd recovery from chloride-rich PGM leachate simulants, demonstrating the combined advantages of TA-disulfide coordination chemistry, broad HCl tolerance, multi-metal Pd selectivity, regenerability, and fixed-bed compatibility.

1. Introduction

Platinum group metals (PGMs), particularly Pd, Pt, and Rh, have various applications, including in jewelry, catalysts, and high–tech devices. Among these, automotive catalytic converters (ACCs) are the dominant consumer of PGMs, accounting for ~65% of global PGM demand [1,2]. Despite ongoing advances, global PGMs recycling performance from end–of–life ACCs remains modest, and according to the U.S. Geological Survey report [3], in 2021, only about 28% of the total global PGMs supply came from recycling. Notably, recycling requires only 1–1.5% of the energy consumed by primary mining [4,5], offering a more sustainable approach to meet future PGMs demand.

Recovery of these metals from secondary resources is carried out primarily through pyrometallurgical and hydrometallurgical methods. While pyrometallurgical processes are effective, they are highly energy–intensive and generate significant emissions, limiting their sustainability [6]. In contrast, hydrometallurgical approaches require less energy, milder operating conditions, and safer waste management [7]. In hydrometallurgical PGM recovery, the initial step is typically HCl-based acid leaching, which dissolves Pt, Pd, and Rh from the solid catalyst into the liquid phase as stable anionic chloro-complexes [8]. Under these conditions, Pt, Pd, and Rh are converted into stable anionic chloro–complexes, predominantly $[PdCl_4]^{2-}$, $[PtCl_6]^{2-}$, and $[RhCl_6]^{3-}$ [9–11]. These species coexist with a range of co–dissolved elements, including base metals (e.g., Fe, Zn) and rare earth elements (e.g., Ce) originating from the catalyst washcoat and substrate. The subsequent separation from cationic impurities is straightforward but achieving intra–PGMs separation remains a significant challenge due to their

* Corresponding authors.
E-mail addresses: anobahar@ua.pt (A. Nobahar), nicolas.schaeffer@ua.pt (N. Schaeffer).

https://doi.org/10.1016/j.cej.2026.178604
Received 19 May 2026; Received in revised form 18 June 2026; Accepted 19 June 2026
Available online 20 June 2026

closely related chemistries and the stability of their chloro–complexes.

An important insight for designing selective PGMs separation processes is the strong affinity of Pd and Pt for sulfur–containing ligands. Both Pd(II) and Pt(II/IV) are "soft" Lewis acid centers that form very stable complexes with soft base donor atoms such as sulfur [12]. As a result, sulfur–bearing extractants and adsorbents are extensively employed in hydrometallurgical systems for the recovery of these metals from chloride media [13]. In particular, sulfur–functionalized materials, including thiols, dithioethers, and thiourea–based resins demonstrated high binding capacities [14–16]. However, despite their effectiveness, these systems generally exhibit limited selectivity as both metals interact strongly with sulfur donors under chloride conditions. This often results in the co–extraction of Pd and Pt, hindering efficient intra–PGMs separation. The challenge is further compounded by the similar coordination environments and comparable thermodynamic stability of Pd and Pt chloro–complexes. Consequently, ligand systems that exploit differences in coordination kinetics are required for selective Pd/Pt separation.

Among the sulfur–bearing molecules, those containing disulfide bonds (–S–S–) are of particular interest owing to their specific interaction pathways with these metals. Pd and Pt can both interact with disulfides either by directly coordinating to the intact –S–S– bond, yielding mono– or binuclear adducts, or by promoting cleavage of the disulfide linkage through oxidative addition, disproportionation, or polarization processes [17]. In chloride media, Pd, being more kinetically labile, shows a higher tendency to form S,S′–binuclear Pd(II) complexes that can be accompanied by partial disulfide bond scission, leading to the formation of Pd–thiolate species [18–21]. By contrast, Pt is frequently present as the more inert $[PtCl_6]^{2-}$ complex, which exhibits slower ligand substitution and more limited ability to participate in coordination or redox interactions with disulfides [20–22].

A representative disulfide–bearing ligand is thioctic acid (TA) – also known as α–lipoic acid, a naturally occurring organosulfur compound. TA is commercially available in high purity, readily photodegradable and biodegradable, non–persistent in the environment, and exhibits low toxicity, making it an environmentally benign candidate for industrial applications [23,24]. Its strained 1, 2–dithiolane ring provides a soft S–donor framework that, upon coordination or mild reductive opening, can enable the formation of strong chelates with Pd in preference to other metals. These structural features enable TA to preferentially interact with soft metal ions such as Pd(II) and to bind strongly to soft metal surfaces. Consequently, TA was widely investigated as a capping or stabilizing ligand for soft metal nanoparticles (e.g., Pd, Au, and Ag), as well as for biomedical nanocarriers [25–28]. Nevertheless, its potential for selective Pd(II) recovery in complex, multi–metallic hydrometallurgical leachates received limited attention.

To the best of our knowledge, the most closely related study is that of Trieu et al. [29], which reported Pd and Au adsorption on TA–functionalized ZrO_2. This work demonstrated the potential of TA for Pd adsorption but was limited to simplified single– or binary–metal systems and did not examine realistic multi–metallic ACC leachates or intra–PGMs selectivity. Moreover, the TA immobilization in that study relied on carboxylate linkages, which proved highly susceptible to hydrolytic cleavage in strongly acidic media (HCl > 1 M) [29]. Even when a phosphonate intermediate (alendronic acid) was introduced to improve anchoring, concerns about long–term hydrolytic stability persist under the highly acidic, chloride–rich conditions typical of industrial hydrometallurgical processes [30].

In previous works on sulfur–functionalized adsorbents, most reported systems suffer from limited selectivity between Pd and Pt and are typically evaluated under mild acidity or simplified metal compositions. Their performance under strongly acidic, chloride–rich environments representative of PGM hydrometallurgical leachates remains largely unexplored. Furthermore, continuous–flow validation is rarely addressed, limiting assessment of practical applicability. In this work, these limitations are addressed by developing a robust TA–functionalized adsorbent via silane–mediated immobilization on a silica support. This approach enables stable covalent attachment and improves resistance to hydrolytic degradation under strongly acidic conditions. The material was evaluated for selective Pd(II) adsorption from HCl–based multi–metallic solutions representative of ACC leachates under industrially relevant conditions (high acidity, elevated chloride, and competitive matrices) in both batch and continuous modes. Unlike most previous studies, which were limited to single–metal or mild systems, this work demonstrates selective Pd recovery under realistic hydrometallurgical conditions, providing a more application–oriented assessment of TA–based adsorbents.

2. Materials and methods

Detailed information on the reagents and characterization techniques used for the adsorbent is provided in the "Methodology" section of the Supporting Information.

2.1. Thioctic acid immobilization on silica gel

Immobilization of TA onto silica gel was carried out as outlined in Fig. 1 and described below:

2.1.1. Step 1. Amino functionalization with APTMS

One gram of pretreated silica (overnight in concentrated HCl) was dispersed in 100 mL of dry toluene (dried over 4 Å molecular sieves) in a round–bottom flask. Subsequently, 2 mL of (3–aminopropyl)trimethoxysilane (APTMS) was added dropwise under continuous stirring. The mixture was refluxed under a nitrogen atmosphere, then sealed and stirred at room temperature for 24 h. The resulting APTMS–functionalized silica (Si–NH_2) was filtered, washed four times with toluene followed by absolute ethanol, and dried at 60 °C overnight.

2.1.2. Step 2. Activation of TA and coupling with Si–NH_2

TA (1.25 g, 6 mmol) was dissolved in 125 mL of dry dichloromethane (DCM) (dried over 3 Å molecular sieves). N, N′–dicyclohexylcarbodiimide (DCC) (1.65 g, 8 mmol) was added directly to the DCM solution. In parallel, N–hydroxysuccinimide (NHS) (0.925 g, 8 mmol) was dissolved in 5 mL of dry acetonitrile and slowly added to the solution under stirring. The mixture was stirred in the dark at room temperature for 60 min to activate the carboxyl group and form the NHS ester.

The NHS–activated TA solution was mixed with the Si–NH_2 prepared in Step 1. The mixture was stirred at room temperature for 24 h in the dark. The product was recovered by filtration and extensively washed with DCM, methanol, and ethanol to remove unreacted species and byproducts. The final product, TA@Si, was dried at 60–80 °C in an oven.

2.2. Batch adsorption–desorption studies

Batch adsorption tests were conducted in 2 mL Eppendorf tubes containing 1.8 mL of a synthetic multi–metal solution containing Fe, Zn, Ce, Pt, Pd, Rh, each at (20 ± 2) mg·L^{-1} prepared in either 0.2 or 3 M HCl, with an adsorbent dosage of 1 g·L^{-1}. The suspensions were agitated at 1500 rpm at 303 K for 3 h using an Eppendorf ThermoMixer. All experiments were performed in duplicate, unless specified otherwise. A control sample without TA@Si, with the same number of replicates, was included in all tests to account for non–adsorptive losses. The influence of HCl molarity on PGMs adsorption was examined by varying HCl concentration from 0.05 to 10.00 M. Kinetic adsorption experiments were conducted in parallel using identical Eppendorf tubes over a 24 h period. At each predefined time interval, two tubes were withdrawn as replicates for metal analysis. The effect of initial metal concentration was studied by performing adsorption studies in multi–metallic solutions containing 5.0 ± 0.4, 10 ± 1, 20 ± 2, 30 ± 2, 40 ± 3, 60 ± 4, 80 ± 5 and (100 ± 7) mg·L^{-1} of Pd, Pt, Rh, Ce, Zn, and Fe. Temperature

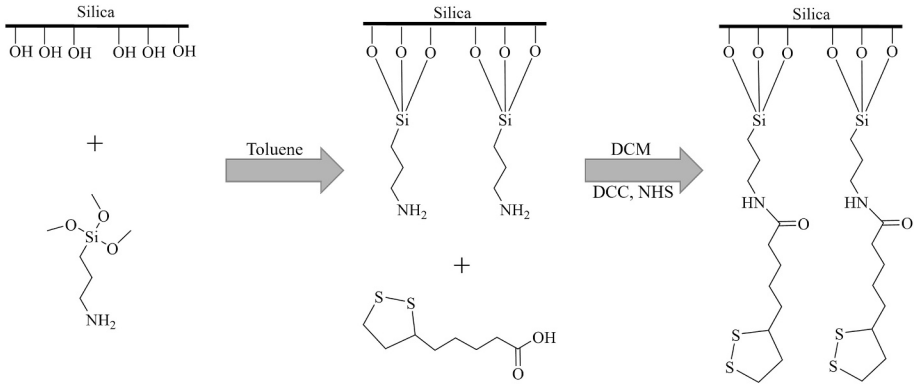

Fig. 1. The synthesis route of thioctic acid functionalized silica gel.

effects were studied at 303, 313, 323, and 333 K under otherwise identical conditions.

For batch desorption studies, TA@Si loaded with Pd and Pt obtained under optimized adsorption conditions (0.2 M HCl, 303 K, 3 h contact time) was used. Desorption was carried out using different eluents, including HCl (1.0, 2.0, and 4.0 M), NaSCN (0.2, 0.5, and 1.0 M), and thiourea (0.2, 0.5, and 1.0 M in 0.5 M HCl). Experiments were conducted in triplicate at 303 K with agitation at 1500 rpm for 3 h. After treatment, samples were filtered, and the metal concentrations were determined.

Successive adsorption–desorption cycles were performed using the same TA@Si. Each adsorption cycle was carried out with a fresh multi–metallic solution, while desorption was performed using the same 1 M thiourea (TU) + 0.5 M HCl solution throughout all cycles. In all experiments, the solid–to–liquid ratio was maintained at 1 $g{\cdot}L^{-1}$.

2.3. Continuous–flow fixed–bed column studies

To evaluate the scalability and dynamic selectivity of TA@Si, continuous–flow fixed–bed column experiments were performed. A plastic syringe (internal diameter 0.5 cm) was packed with 0.5435 g of TA@Si (with average particle size of 0.2–0.5 mm), corresponding to a bed height of 4 cm (bed volume ≈ 0.785 cm^3), and used as the column. Both ends of the packed bed were secured with glass wool to prevent material loss and ensure uniform flow. Prior to operation, the column was preconditioned with 0.2 M HCl to fully wet the sorbent bed and remove trapped air. The column was placed in a thermostatic water bath (ME–18 *V* Visco–Thermostat, Julabo) maintained at 30 °C (± 0.01 °C) to ensure constant operating conditions (Fig. S1).

A synthetic multi–metallic solution containing (50 ± 5) $mg{\cdot}L^{-1}$ of Fe, Zn, Ce, Pt, Pd, and Rh in 0.2 M HCl was pumped upward using a peristaltic pump at a constant flow rate of 1 $mL{\cdot}min^{-1}$ (empty–bed contact time ≈ 0.785 min). The experiment was conducted for 10 h (total processed volume = 600 mL, ≈ 764 bed volumes). Following column saturation, desorption was carried out in the same setup using a stepwise elution strategy with eluents of increasing complexation strength. The column was sequentially treated with 0.01 M TU in 0.5 M HCl and 1 M TU in 0.5 M HCl, all at a flow rate of 1 $mL{\cdot}min^{-1}$. The desorption stage was conducted for 4 h (total processed volume = 240 mL, ≈ 306 bed volumes). Effluent samples were collected at 10 min intervals throughout the column operation (including both adsorption and desorption stages) and analyzed by ICP–OES.

3. Results and discussion

3.1. Structural and spectroscopic characterization of TA@Si

To confirm the successful covalent immobilization of TA on silica, FTIR, Raman, solid–state ^{13}C NMR spectroscopy, and CHNS elemental analysis were performed. FTIR spectra of silica (Si), silica with APTMS linker (Si–NH_2), and TA–functionalized silica (TA@Si) are presented in Fig. 2–A. The spectrum of TA@Si exhibited two characteristic peaks at 1553 and 1649 cm^{-1}, corresponding to the amide II (N—H bending and C—N stretching) and amide I (C═O stretching) vibrations, respectively. These peaks confirm the successful immobilization of TA onto Si–NH_2 [31,32]. A peak at 1632 cm^{-1}, assigned to the bending vibration of physisorbed water, was observed in the spectra of both bare Si and Si–NH_2 [33]. All samples retain the silica framework bands at 1080, 811, and 510 cm^{-1} (Si–O–Si asymmetric stretch, Si–O–Si symmetric stretch, and Si—O bend).

Raman spectroscopy (Fig. 2–B) further corroborates the successful TA grafting. Bare silica is essentially featureless, whereas Si–NH_2 shows aliphatic C—H stretching bands in the region 2850–2960 cm^{-1} (centered ~2931 cm^{-1}), attributed to the propyl linker [34]. Upon TA coupling (TA@Si), these C—H bands intensify, and TA–characteristic sulfur modes appear: the 1, 2–dithiolane ν(S—S) near ~510 cm^{-1} and ν(C—S) bands within ~630–700 cm^{-1}, absent in Si–NH_2 and matching the fingerprint of pure TA. In addition, a band at ~1440 cm^{-1} ($\delta(CH_2)$ scissoring vibration) grows from Si–NH_2 to TA@Si, indicating increased aliphatic content from the TA layer. In the carbonyl region, TA@Si shows an amide I band at approximately 1650–1670 cm^{-1}, consistent with amide formation between TA and surface amines [35,36] and in agreement with FTIR results.

The functionalization was further confirmed by solid–state ^{13}C CP–MAS NMR spectroscopy. Fig. 2–C displays the spectra of pure TA, Si–NH_2, and TA@Si. The presence of the APTMS linker on the silica surface is clearly evidenced by three characteristic signals assigned to the propyl chain methylene carbons, observed at 7.39 ppm (C1), 25.60 ppm (C2), and 39.31 ppm (C3), consistent with literature values [31,37]. In the spectrum of pure TA, a distinct peak at 163.98 ppm corresponds to the carbonyl carbon (C=O) of the carboxylic acid group [38]. Upon conjugation to the Si–NH_2 surface, this peak shifts to 160.10 ppm, reflecting a change in the chemical environment of the carbonyl and indicating the formation of an amide bond between the terminal amine of APTMS and the carboxylic group of TA. In the aliphatic region (20–45 ppm), the pure TA spectrum exhibits three peaks assigned to methylene carbons within the eight–membered ring and side chain, including those adjacent to the disulfide bridge (–CH_2–S–S–CH_2–) [38]. In the TA@Si spectrum, this region shows broader features. This increased multiplicity and line broadening are expected for organic molecules immobilized on heterogeneous silica surfaces, where restricted mobility and varied local binding geometries lead to slightly different 13C chemical environments [39]. Notably, the peak at 39.31 ppm, which originates from the CH_2 group adjacent to the –NH_2 in APTMS, likely overlaps with methylene signals from TA, particularly those near the disulfide linkage.

CHNS elemental analysis (Table S1) of TA@Si showed the presence of ~3% N, confirming the incorporation of the APTMS linker, while 2.4% S was attributed to the dithiolane ring of TA, providing direct

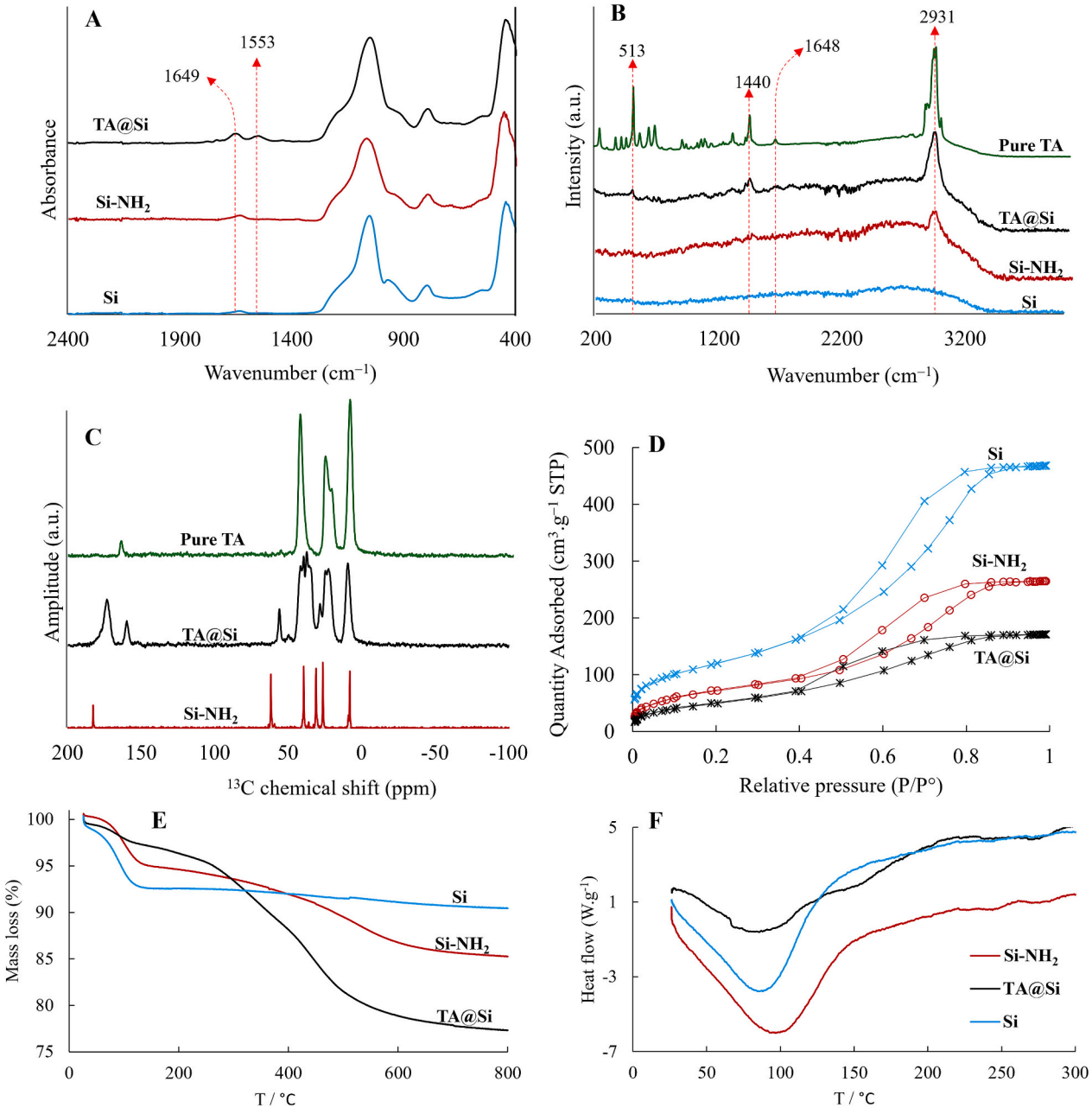

Fig. 2. Characterization of silica gel (Si) before and after functionalization with APTMS (−NH_2) and thioctic acid (TA): **(A)** FTIR spectra, **(B)** Raman spectra, **(C)** solid-state ^{13}C CP–MAS NMR spectra, **(D)** N_2 adsorption–desorption isotherms, **(E)** TGA curves, and **(F)** DSC heat-flow curves.

evidence of its attachment. The elevated carbon and hydrogen contents are consistent with the added organic layers.

The N_2 adsorption–desorption isotherms of Si, Si–NH_2, and TA@Si showed Type IV behavior, confirming the mesoporous nature of all samples (Fig. 2–D). The marked increase in adsorbed volume at intermediate relative pressures is attributed to capillary condensation within mesopores [40,41]. As shown in Table S2, surface functionalization with APTMS and TA results in a progressive decrease in BET surface area and total pore volume, reflecting partial pore blocking and reduced pore accessibility arising from the grafted organic layers. Despite this reduction, the overall isotherm shape and pore–size distribution remain characteristic of mesoporous materials, indicating that the silica framework is preserved after functionalization [42].

Finally, TGA profiles (Fig. 2–E) further confirm the successful organic functionalization of silica. Bare Si showed only a small mass decrease, mainly associated with adsorbed water and surface silanol condensation, whereas Si–NH_2 and TA@Si exhibited progressively higher mass losses due to the decomposition of grafted APTMS and TA organic moieties. The larger mass loss observed for TA@Si confirms the increased organic loading after TA immobilization. The DSC curves (Fig. 2–F) show broad thermal events below ~150 °C, mainly related to moisture/solvent removal and surface-bound species. No major thermal events were observed below 300 °C, consistent with the thermal stability observed by TGA.

3.2. Metal adsorption tests

Following the successful immobilization of TA on silica gel, the prepared material was evaluated as an adsorbent for the selective uptake of metals from HCl–based synthetic multi–metallic solutions, designed to simulate chloride leachates relevant to hydrometallurgical processing.

3.2.1. Effect of HCl concentration and metal adsorption kinetics

The effect of HCl concentration on metal uptake by TA@Si was evaluated over a wide acidity range (0.05–10 M HCl). As shown in Fig. 3–A, the adsorption of both Pd and Pt is strongly dependent on HCl concentration. Maximum uptake for both metals was observed at the lowest acidity tested (0.05 M), followed by a progressive decrease with increasing HCl concentration. This decrease in adsorption is attributed to the stabilization of Pd and Pt chloro-complexes by excess chloride ions, which shifts the equilibrium toward fully chlorinated anionic species ($[PdCl_4]^{2-}$ and $[PtCl_6]^{2-}$) and reduces their susceptibility to ligand exchange with the sulfur donor groups on the TA@Si surface [43]. The adsorption mechanism and the origin of the observed Pd selectivity are discussed in further detail in Section 3.3.2. At higher acidities, Pt adsorption remains negligible, while Pd retains measurable uptake even at 10 M HCl, giving a separation factor $\alpha_{Pd/Pt} > 28$ (Eq. S1) for HCl acidities above 4 M due to the suppression of Pt uptake (Fig. 3–A). This difference reflects their distinct solution speciation and kinetic behavior. Pt is predominantly present as the kinetically inert $[PtCl_6]^{2-}$ complex, which resists ligand exchange, whereas Pd exists mainly as more substitution–labile $[PdCl_4]^{2-}$ species, allowing Pd adsorption to persist under highly acidic conditions [17,20,21]. In contrast, Rh and the base metals (Fe, Zn, Ce) showed negligible adsorption across all HCl concentrations tested.

The chemical stability of TA@Si in acidic media was assessed by immersing the material in 0.2 and 3 M HCl solutions and stirring for seven days. The acid–pretreated samples were then directly used for metal adsorption from multi–metallic solutions prepared at the same respective HCl concentrations and compared in parallel with fresh TA@Si (Fig. S2). The results show that prolonged exposure to the tested acidic environments does not compromise the material's metal adsorption performance.

Furthermore, the adsorption kinetics of metals from a 0.2 M HCl solution onto TA@Si (1 $g{\cdot}L^{-1}$) were evaluated over a 24 h period. Both Pd and Pt exhibited rapid adsorption within the first 30 min, followed by a slower approach to equilibrium, which was reached at ~180 min (Fig. 3–B). Kinetic modelling further supported these trends (Table S3). For Pd, the experimental and calculated adsorption capacities ($q_{e,exp}$ = 15.28 $mg{\cdot}g^{-1}$; $q_{e,cal}$ = 15.20 $mg{\cdot}g^{-1}$) were in close agreement under the pseudo–second order (PSO) model (Eq. S3), with a high correlation coefficient (R^2 = 0.96). In contrast, the pseudo–first order (PFO) model (Eq. S2) gave a poorer correlation (R^2 = 0.71). Similarly, Pt adsorption kinetics were better described by the PSO model (R^2 = 0.99), with calculated q_e values in closer agreement than for PFO. These results indicate that chemisorption is the dominant mechanism, suggesting specific interactions between Pd/Pt chloro–complexes and sulfur donor sites of TA@Si [44,45]. Moreover, the rate–limiting step of Pd and Pt adsorption is the chemical complexation process itself, involving ligand substitution and activation of the disulfide bond to form Pd—S or Pt—S coordination species, rather than mass transfer or diffusion [19,22].

3.2.2. Isotherm studies

Adsorption isotherms for the different metals on TA@Si were measured at 0.2 M and 3 M HCl. In both media, Pd adsorption capacity increased progressively with the initial concentration (Fig. 4–A, C), while Pt adsorption exhibited only a modest increase with concentration (Fig. 4–B, D). Notably, no measurable uptake was observed for the other tested metals (Rh, Fe, Zn, and Ce).

Equilibrium adsorption data for Pd and Pt on modified silica were fitted to Langmuir (Eq. S4), Freundlich (Eq. S5), Sips (Eq. S6), and Temkin (Eq. S7) isotherm models (Fig. 4–A–D, Table S4). The Sips model provided the best fits (R^2 = 0.99). For Pd, the maximum adsorption capacity (q_{max}) decreased from (49.51 ± 12.37) $mg{\cdot}g^{-1}$ at 0.2 M HCl to (29.02 ± 1.74) $mg{\cdot}g^{-1}$ at 3 M HCl (Table S4). The Sips heterogeneity exponent (n = 0.72–0.83) deviates from unity, indicating apparent energetic heterogeneity, which in this system is attributed to variations in site accessibility and adsorption strength induced by solution acidity, metal speciation, and surface coverage [46]. The Temkin model also provided an excellent fit for Pd (R^2 = 0.99); its constant b_T rose from 0.33 to 0.48 kJ mol^{-1} with increasing acidity, consistent with the Temkin framework, in which the apparent adsorption energy varies with coverage and solution conditions [46,47]. The Langmuir model yielded inferior fits (R^2 = 0.97–0.99) (Table S4), indicating minor deviations from ideal monolayer adsorption on energetically homogeneous sites. The Freundlich model gave the poorest fit ($R^2 \leq 0.93$). For Pt, the Sips model again provided the best fit (R^2 = 0.96–0.97), with q_{max} decreasing from (7.06 ± 1.87) $mg{\cdot}g^{-1}$ at 0.2 M HCl to (2.06 ± 0.56) $mg{\cdot}g^{-1}$ at 3 M. The heterogeneity parameter (n = 0.80 at 0.2 M) indicates moderate energetic heterogeneity of the adsorption sites. The elevated value obtained at 3 M HCl (n = 2.59) should be interpreted with caution, as the very low Pt adsorption capacity under these conditions reduces the reliability of the fitted parameter and may artificially inflate the heterogeneity exponent [46] (Fig. 4–C, D, Table S4).

The superior Sips and Temkin fits and the acidity–driven drop in q_{max} indicate apparent energetic heterogeneity arising from acidity– and coverage–dependent interactions. This behavior is consistent with competitive adsorption and modulation of binding strength by solution conditions, as captured by these models [46,47].

Importantly, the maximum Pd adsorption capacity closely correlates with the TA loading estimated from elemental analysis, indicating that adsorption is primarily governed by the availability of TA–derived sulfur

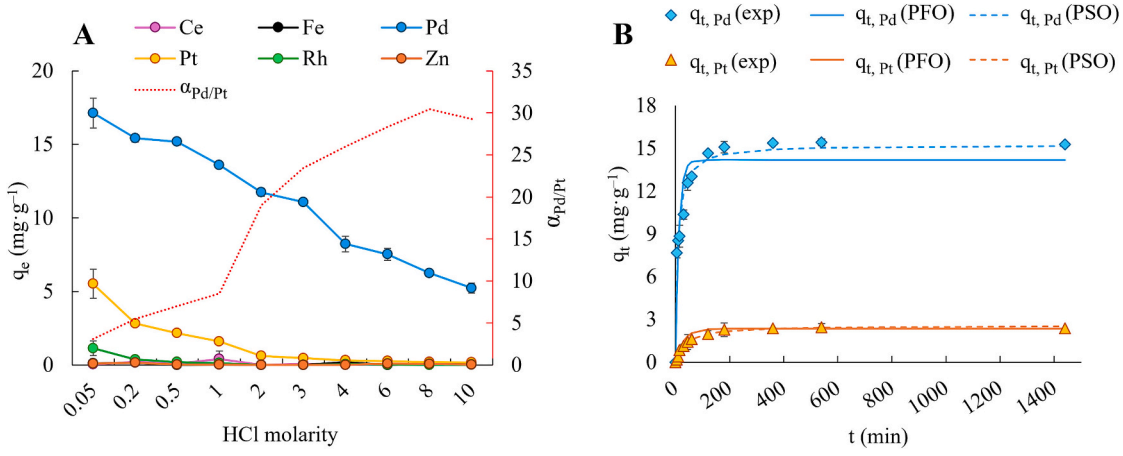

Fig. 3. (A) Influence of HCl concentration on the adsorption of different metals from synthetic multi–metallic solutions by TA@Si (contact time of 180 min). **(B)** Adsorption kinetics of Pd and Pt by TA@Si with nonlinear pseudo–first–order (PFO) and pseudo–second–order (PSO) model fits. Experimental conditions: TA@Si dosage of 1 $g{\cdot}L^{-1}$, temperature at 303 K, multi–metallic solution containing (20 ± 2) $mg{\cdot}L^{-1}$ of each metal in 0.2 M HCl.

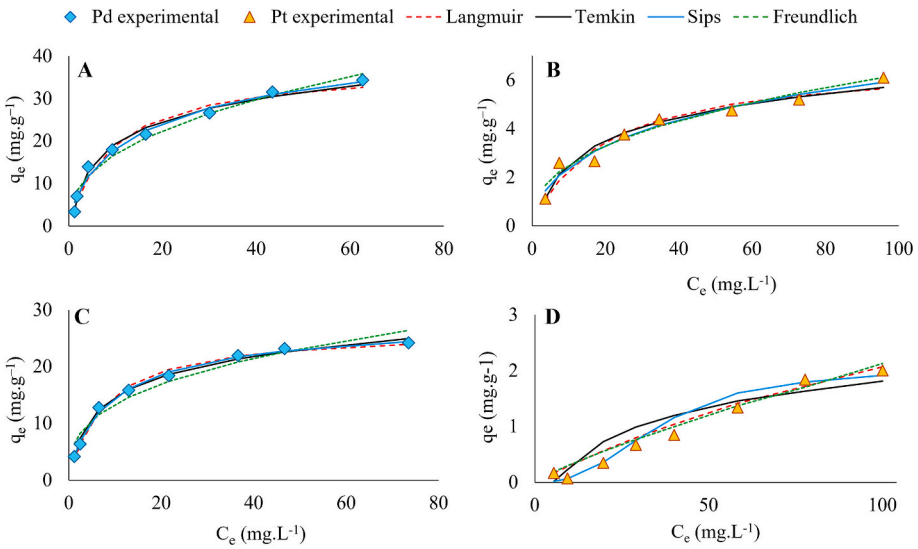

Fig. 4. Equilibrium adsorption isotherms of Pd and Pt on TA@Si as a function of initial metal concentration, with nonlinear fitting to Langmuir, Freundlich, Temkin, and Sips models. Results obtained in 0.2 M HCl are shown for (A) Pd and (B) Pt, while those obtained in 3 M HCl are shown for (C) Pd and (D) Pt. Experimental conditions: TA@Si dosage of 1 g·L^{-1}, temperature at 303 K, and contact time of 180 min.

sites. Based on the sulfur content in Table S1 (2.41 wt%), approximately 0.376 mmol of TA is present per gram of material, while the maximum Pd uptake at 0.2 M HCl reaches 49.51 mg·g^{-1} (≈0.465 mmol·g^{-1}). The near one–to–one correspondence between these values suggests high utilization of active sulfur sites, with Pd binding occurring predominantly at TA-derived functionalities. The slightly higher Pd uptake relative to TA loading further indicates that multiple coordination modes, including mono– and bidentate Pd—S interactions, contribute to the overall adsorption capacity, consistent with the proposed mixed Pd–S/Cl coordination environment [17,19].

3.2.3. *Comparative evaluation of adsorption performance under acidic chloride conditions*

The performance of TA@Si was benchmarked against reported adsorbents under comparable conditions (Table 1). From a kinetic perspective, TA@Si exhibits substantially faster uptake than most reported systems. For example, Zhang et al. [48] reported high Pd selectivity over Pt ($\alpha_{Pd/Pt}$ = 64.5) using sulfur–functionalized cellulose under mild acidic conditions (pH 0–3, ≤1 M HCl); however, equilibrium was reached only after prolonged contact times (~12–24 h), likely due to diffusion limitations and restricted site accessibility. Similarly, thiol–functionalized mesoporous silica systems required ~7 h to reach equilibrium for both Pd and Pt adsorption, more than twice the time observed in this study [14]. In our previous work, Pd adsorption onto disulfide–rich feathers required ~6 h to reach equilibrium, attributed to intraparticle diffusion limitations within the dense keratin matrix, where mass transfer governed the overall rate [49]. In contrast, the kinetics observed here are comparable to those reported for TA–modified ZrO_2, where equilibrium was achieved within ~200 min for Pd and Au adsorption [29].

The stability and effectiveness of sulfur–based functionalities in acidic media were not sufficiently evaluated in the literature, as many studies are limited to simple–metal systems or to mild acidity (typically <1 M HCl) [13,29,48,50,51], thereby limiting their applicability to real hydrometallurgical streams. Even when tested in chloride media, selectivity is often inadequate (Table 1). For instance, thiourea–based

Table 1
Comparison of Pd and Pt adsorption performance of TA@Si with reported sorbents in acidic chloride media, including adsorption capacity (q_e) and selectivity ($q_{e,Pd}/q_{e,Pt}$) under comparable conditions.

Functional group/ active site	Support	Feed composition	Medium/ condition	q_e (mg·g^{-1})		$q_{max,Pd}$	$\alpha_{Pd/Pt}$	$q_{e,Pd}/q_{e,Pt}$	Equilibrium time (h)	Ref.
				Pd	**Pt**					
Thioctic acid disulfide	Mesoporous silica	Pd, Pt, Rh, Fe, Zn, Ce	0.2 M HCl 3 M HCl 10 M HCl	15.4 11.1 5.2	2.8 0.5 0.2	49.5 29.0 –	5.6 23.6 31.2	5.5 22.2 26	3	This work
Thioctic acid disulfide	ZrO_2 nanoparticles	Pd, Au	3 M HCl	6.3	–	6.3	–	–	~3	[29]
2–aminothiophenol	Cellulose	Pd, Pt, base metals	pH 1.0	163.2	19.8	163.2	64.5	~6.36	~12–24	[48]
Bis–(2–picolyl)amine	Polymeric resin	Pd, Pt, Rh,	3 M HCl	0.5	0.5	–	~20	~1.2	>9	[43]
–	Mesoporous Carbons	Pd, Pt, Au	1 M HCl	35	58.5	95.8	–	~0.6	18	[56]
2–aminophenyl disulfide	Mesoporous silica	Pd, Pt	0.5 M HCl	–	–	26.6	Very high (NR)	~5.4	0.1	[53]
3–mercaptopropyl	Mesoporous silicas	Pd	pH 1.0	190	–	190	–	–	3	[54]
Sulfur heteroatoms modified crown ether	crosslinked polymer resin	Pd, Pt	6 M HCl	177.7	66.3	212	–	~2.7	6–12	[57]
Dichloro–thioamide	Polyethyleneimine	Pd, Pt, Au, base metals	pH 1	886	1021	886	–	~0.9	~20	[55]
Thiol	Mesoporous silica	Pd, Pt	pH 4	10.4	17.9	170	–	~0.6	~8	[14]
Phosphine oxide	Macroporous polyacrylic resin	Pt, Pd, Rh, Cu	Not reported	28.6	30.3	28.6	–	~0.94	~2	[58]

ion–exchange resins exhibit limited Pd/Pt discrimination, resulting in significant co–adsorption in multi-metallic solutions across a wide acidity range (0.1–9 M HCl) [43]. Similarly, thiol–functionalized silica shows negligible selectivity between Pd and Pt [14], while electrostatic–based adsorbents lose effectiveness at high acidity due to competitive binding with chloride ions [52].

In terms of adsorption capacity and selectivity, TA@Si falls within the upper range reported for disulfide–based systems. Disulfide–functionalized silica materials, such as 2–aminophenyl disulfide, typically exhibit capacities of 10–26 $mg{\cdot}g^{-1}$ [53], while TA–modified ZrO_2 shows a lower capacity of ~6.3 $mg{\cdot}g^{-1}$ under acidic conditions (pH ≈ 0.3) [29]. Although higher selectivity toward Pd over Pt has been reported in some cases, such as the work by Losev et al. [53], the evaluation of selectivity under competitive and strongly acidic conditions remains limited. In contrast, thiol–functionalized adsorbents generally achieve substantially higher capacities, including 163 $mg{\cdot}g^{-1}$ for 2–aminothiophenol–functionalized cellulose [48], ~190 $mg{\cdot}g^{-1}$ for thiol–modified silica [54], and up to 886 $mg{\cdot}g^{-1}$ for dichloro–thioamide–functionalized polyethyleneimine [55]. However, this apparent advantage is often accompanied by poor selectivity, as thiol groups exhibit strong but non–specific affinity toward multiple PGMs, particularly Pd and Pt.

As summarized in Table 1, most reported studies were conducted under relatively mild conditions and do not reflect the behavior of adsorbents under strongly acidic environments relevant to hydrometallurgical processing. In contrast, TA@Si maintains high selectivity and stability toward Pd across a wide range of HCl concentrations. Although the adsorption capacity decreases with increasing acidity, the selectivity remains consistently high, highlighting the robustness of the material under industrially relevant conditions.

3.3. Adsorption mechanism

3.3.1. Thermodynamics

The thermodynamics of metal adsorption onto TA@Si were investigated by measuring adsorption efficiencies in 0.2 and 3 M HCl at 303, 313, 323, and 333 K. As shown in Fig. 5–A and B, increasing the temperature enhanced the adsorption capacities of Pd and Pt at both acid concentrations. In contrast, adsorption of the base metals (Ce, Fe, Zn) remained negligible, while only a slight increase was observed for Rh. However, the temperature-induced increase was more pronounced for Pt, likely because higher temperature facilitates desolvation and ligand-substitution processes for the kinetically inert Pt chloro-complexes. As a result, Pd/Pt selectivity decreased at higher temperatures, indicating that lower adsorption temperatures are more favorable for selective Pd recovery.

The thermodynamic parameters obtained from the van't Hoff analysis (Eq. S8) provide insight into the nature of Pd and Pt adsorption onto TA@Si; the corresponding plots are shown in Fig. 5–C and D and the extracted values are summarized in Table 2. The positive enthalpy values (25–26 $kJ{\cdot}mol^{-1}$ for Pd and 37–57 $kJ{\cdot}mol^{-1}$ for Pt) indicate that the adsorption process is endothermic. This is consistent with specific chemical interactions (beyond simple physisorption) between the metal chloro-complexes and the sulfur donor sites of TA@Si [59]. The large positive entropy changes (~88–92 $J{\cdot}mol^{-1}{\cdot}K^{-1}$ for Pd and 109–160 $J{\cdot}mol^{-1}{\cdot}K^{-1}$ for Pt) indicate a gain in disorder, most likely from the release of hydration water and chloride ions upon metal binding, consistent with previous reports on Pd(II) sorption via sulfur donor ligands [60,61]. For Pd, the combination of a moderate ΔH and a favorable ΔS results in consistently negative Gibbs free energy (Eq. S11) values across the studied range, confirming a spontaneous process whose thermodynamic driving force increases with temperature. In contrast, Pt adsorption exhibits larger enthalpic barriers and thus only marginal spontaneity, with a positive ΔG decreasing toward zero at higher temperatures, which explains the experimentally observed increase in uptake. For Pt, increasing the HCl concentration from 0.2 to 3 M magnifies both ΔH and ΔS, reflecting stronger stabilization of metal chloro–complexes in solution and higher desolvation requirements, which, overall, reduce adsorption efficiency. These thermodynamic trends confirm that Pd adsorption is thermodynamically more favorable than Pt adsorption under strongly acidic conditions, rationalizing the observed selectivity of TA@Si.

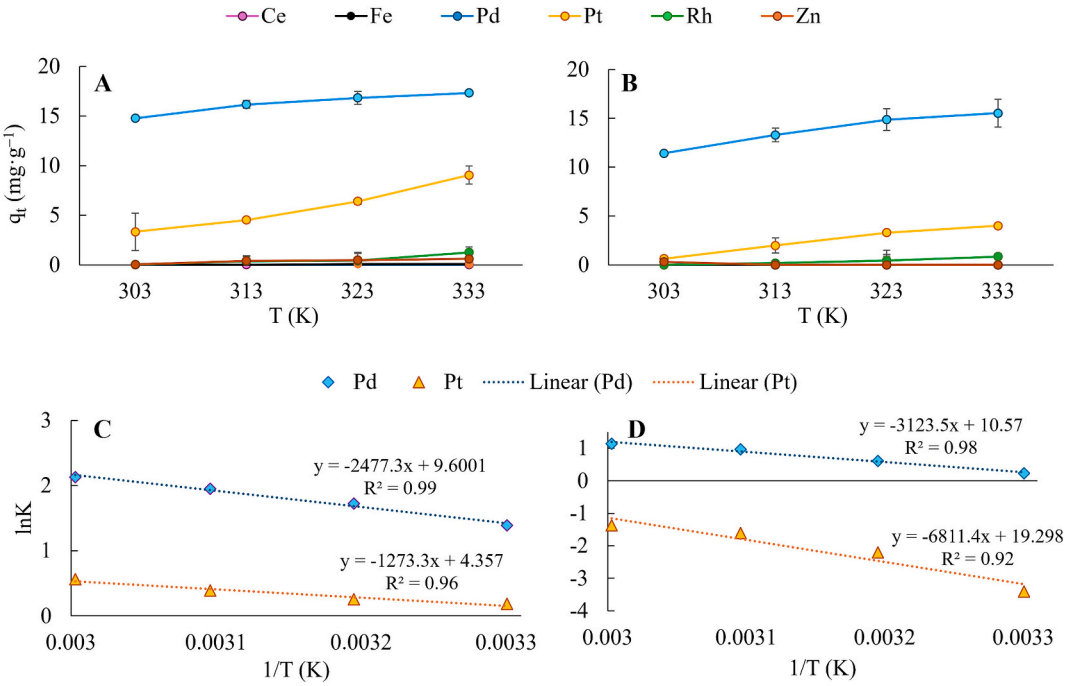

Fig. 5. Effect of temperature on Pd and Pt adsorption from solutions containing **(A)** 0.2 M HCl and **(B)** 3 M HCl. Van't Hoff plots for the thermodynamic analysis of PGMs adsorption by TA@Si from **(C)** 0.2 M HCl and **(D)** 3 M HCl solutions. Experimental conditions: TA@Si dosage of 1 $g{\cdot}L^{-1}$, multi–metallic solution containing (20 ± 2) $mg{\cdot}L^{-1}$ of each metal, and contact time of 180 min.

Table 2
Apparent thermodynamic parameters under optimized experimental conditions for Pd and Pt adsorption on TA@Si at varying temperatures.

		0.2 M HCl		3 M HCl	
Metal		Pd	Pt	Pd	Pt
R^2		0.99	0.96	0.98	0.92
ΔH (kJ.mol^{-1})		25.00 ± 2.49	37.28 ± 1.96	25.97 ± 2.49	56.62 ± 11.92
ΔS (J.mol^{-1}.K^{-1})		92.12 ± 7.85	109.36 ± 6.19	87.88 ± 7.85	160.441 ± 37.57
ΔG (kJ.mol^{-1})	303 K	−2.78 ± 3.44	4.04 ± 2.72	−0.57 ± 3.44	8.59 ± 16.48
	313 K	−3.98 ± 3.50	3.19 ± 2.76	−1.59 ± 3.50	5.72 ± 16.72
	323 K	−4.83 ± 3.55	2.00 ± 2.80	−2.60 ± 3.55	4.32 ± 17.01
	333 K	−5.55 ± 3.61	0.78 ± 2.85	−3.14 ± 3.61	3.81 ± 17.28

3.3.2. *Spectroscopic and structural analyses*

To better rationalize the adsorption behavior and notable selectivity of TA@Si for Pd over Pt, TA@Si was equilibrated with single-metal Pd or Pt solutions at (100 ± 2) mg·L^{-1} and subsequently characterized, ensuring sufficiently high surface loading for spectroscopic analysis.

FTIR spectra of TA@Si before and after Pd or Pt adsorption showed only minor changes (Fig. S3), likely because key metal–sulfur and metal–chloride vibrations occur below ~400 cm^{-1}, outside the reliable mid–IR range. Raman spectra (Fig. 6–A) revealed the appearance of new bands and shifts in existing vibrations after metal binding. In the Raman

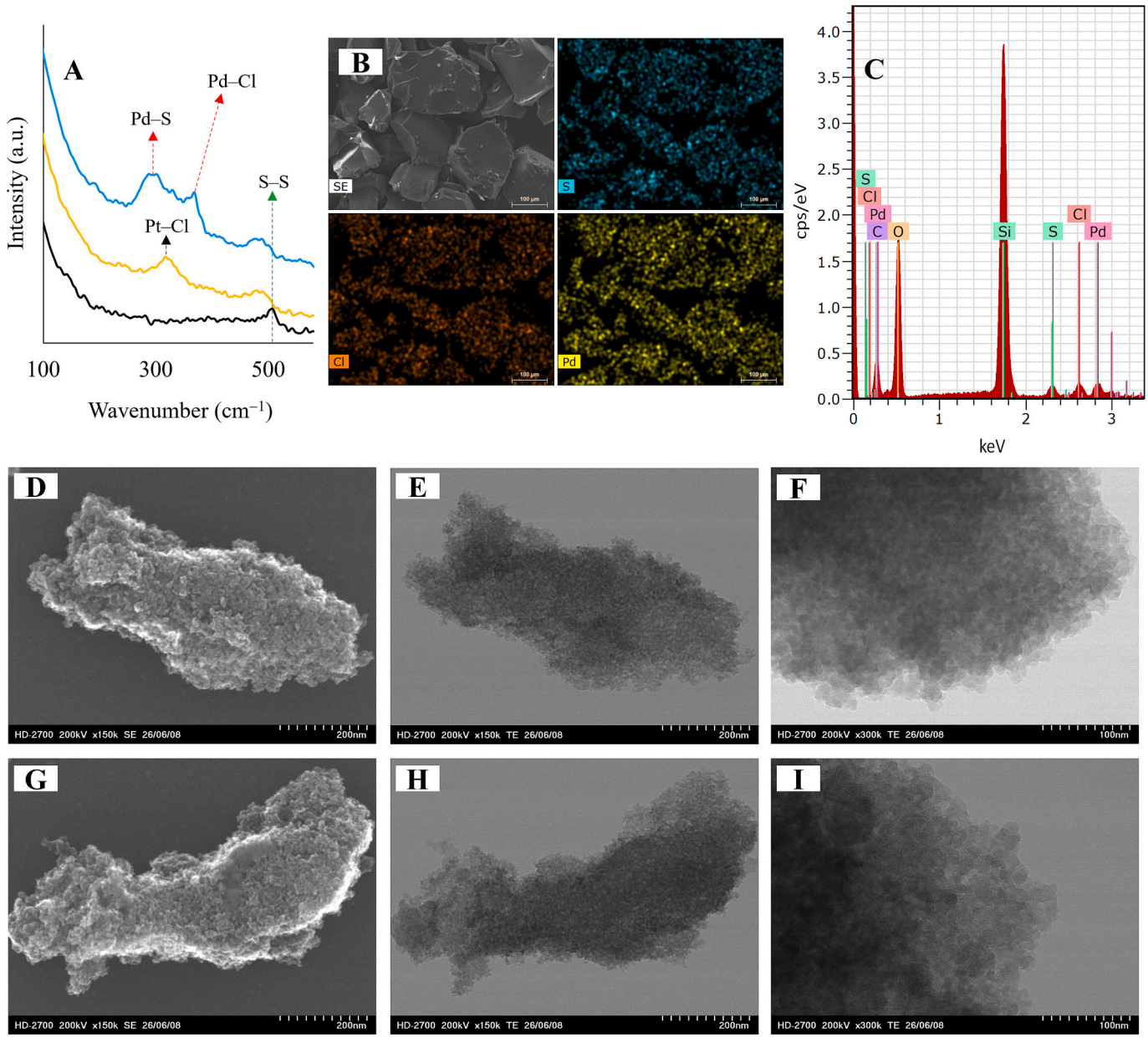

Fig. 6. **(A)** Raman spectra of TA@Si before and after Pd or Pt adsorption. **(B)** SEM–EDS elemental mapping and **(C)** corresponding EDS spectra of TA@Si after Pd adsorption. STEM imaging of TA@Si, **(D-F)** before and **(G-I)** after Pd adsorption. Experimental conditions: TA@Si dosage of 1 g·L^{-1}, single–metal solutions of (100 ± 5) mg·L^{-1} in 0.2 M HCl, contact time of 180 min, and temperature at 303 K.

spectrum of Pd-loaded TA@Si, two new bands appeared at approximately 298 and 368 cm^{-1}, which can be assigned to ν(Pd—S) and ν(Pd—Cl), respectively [62–64]. The first corresponds to the coordination of Pd(II) to the sulfur atoms of TA, while the second reflects the retention of chloride ligands in the coordination sphere. The simultaneous observation of ν(Pd—S) and ν(Pd—Cl) bands suggests that Pd(II) retains part of its chloride coordination sphere upon adsorption, supporting a partial ligand–exchange mechanism rather than complete substitution by sulfur donor groups. For Pt–loaded TA@Si, a new band at ~318 cm^{-1} was observed (Fig. 6–B). This band lies within the typical range of Pt—S stretching vibrations (~300–320 cm^{-1}) as reported for thiolate–Pt species [63,65], but it also overlaps with the region of Pt—Cl stretches observed in cis–[$Pt(NH_3)_2Cl_2$] complexes (312–322 cm^{-1}) [66,67]. Thus, the band may arise from either Pt—S coordination, residual Pt—Cl vibrations, or both, consistent with a scenario in which Pt retains its chloro–complex structure and interacts (weakly) with sulfur donor sites. Moreover, after adsorption of both metals, the band at 507 cm^{-1} shifts to lower wavenumbers (Fig. 6–A). This band corresponds to the disulfide ν(S—S) mode, whose frequency is sensitive to the local bonding environment and decreases when the S—S bond is weakened by electron density redistribution upon metal coordination [68,69]. Importantly, the ν(S—S) band remains clearly observable after Pd adsorption, although shifted to lower wavenumbers. This behavior indicates weakening and polarization of the disulfide bond rather than its complete cleavage. Such metal–sulfur coordination weakens the S—S bond electronically while preserving its integrity, leading to partial metal–thiolate character and asymmetric S—S bonding without ring opening [21,69]. If extensive S—S bond scission had occurred, a significant decrease or disappearance of this vibrational mode would be expected. This observation is consistent with reported coordination modes of Pd(II) with disulfides in chloride media, where mono– or binuclear disulfide complexes can form without requiring full S—S bond cleavage, while thiolate formation typically involves more pronounced structural changes [69]. This interpretation is further supported by the stable adsorption performance observed over multiple adsorption–desorption cycles (see Section 3.4), indicating that Pd and Pt chloro–complexes interact with the disulfide moiety of TA through coordination rather than bond cleavage. The presence of a minor fraction of thiolate-type species arising from partial S—S cleavage cannot be fully excluded on the basis of Raman data alone. Nevertheless, overall, the spectroscopic evidence supports a coordination–induced activation of the disulfide bond, in which Pd(II) forms mixed Pd–S/Cl complexes while preserving the integrity of the S—S linkage, rather than proceeding via complete reductive cleavage to thiolate species.

The XRD patterns of TA@Si before and after Pd adsorption (Fig. S4) showed no discernible changes, with both displaying only a broad reflection characteristic of amorphous silica centered around $2\theta \approx 22°$. No additional peaks corresponding to Pd or Pd–containing crystalline phases were detected. The absence of characteristic metallic Pd reflections ($2\theta \approx 40°$, 46°, 68°) indicates that Pd is not reduced during adsorption but remains highly dispersed, consistent with its coordination as ionic or complex species with surface sulfur donors. SEM–EDS mapping revealed a uniform spatial distribution of S, Cl, and Pd across the TA@Si surface, indicating homogeneous functionalization by TA and uniform Pd uptake (Fig. 6–C, D). Furthermore, STEM images (Figs. 6–D–I) support the preservation of the morphology and porous texture of TA@Si after functionalization and Pd adsorption, with no obvious structural collapse or degradation observed after the adsorption process. The corresponding normalized surface atomic ratios obtained by SEM-EDS (Table S5) show comparable Pd:S (~1:1) and Pd:Cl (~1:1.23) values, qualitatively indicating that Pd is coordinated by sulfur donor groups from TA while retaining chloride ligands in its coordination sphere. These ratios further support the Raman spectra analysis, namely that Pd(II) is immobilized as surface–bound mixed S/Cl complexes formed by partial substitution of chloride ligands from the $[PdCl_4]^{2-}$ precursor.

Finally, XPS spectra of TA@Si before and after Pd adsorption were further analyzed to elucidate the adsorption mechanism and clarify the involvement of TA-derived sulfur sites in Pd uptake (Fig. 7, Table S6). The simultaneous detection of Pd 3d peaks at 338.25 and 343.60 eV, assigned to Pd(II) (Fig. 7–B), together with the Cl 2p doublet, with the Cl $2p_{3/2}$ component at 198.45 eV (Fig. 7–A, Table S6), suggests that Pd is primarily retained as a surface-bound Pd(II)–chloride species. In the high-resolution S 2p spectrum of TA@Si before Pd loading (Fig. 7–D), the dominant S $2p_{3/2}$ component appeared at 164.15 eV, corresponding to disulfide sulfur from the 1,2-dithiolane ring of TA along with a minor low-binding-energy component at 160.95 eV, attributed to reduced or ring-opened thiolate-like sulfur species [70]. The latter likely arises from partial opening of the strained dithiolane ring during synthesis, handling, or unavoidable light exposure [71]. After Pd adsorption, the disulfide S $2p_{3/2}$ component shifted from 164.15 eV to 164.88 eV, while the low-binding-energy component shifted from 160.95 eV to 162.41 eV. The relative intensities of both components did not change substantially (Table S6), indicating that the disulfide bond underwent little to no cleavage upon Pd adsorption. The upward shifts are instead attributed to redistribution of electron density upon coordination with Pd(II), and polarization of the intact S—S bond and formation of surface-anchored mixed Pd–S/Cl complexes. This is supported by the persistence (with shift) of the S—S Raman band after adsorption (Fig. 6–A) and aligns with Pd(II)–disulfide coordination behavior in chloride media, where partial ligand exchange predominates without full reductive cleavage [19,21,72]. Extensive S—S cleavage is not expected under these conditions because cleavage/disproportionation requires a favorable S/S′-binuclear geometry, strong $S\delta^+$–$S\delta^-$ charge separation, and nucleophilic attack, whereas the immobilization of TA on silica restricts conformational freedom and the acidic chloride medium suppresses extensive thiolate formation [19]. Were extensive disulfide cleavage to occur during adsorption-desorption operation, the resulting thiol/thiolate species would be expected to interact strongly with both Pd and Pt, thereby reducing the Pd selectivity observed for the intact TA-functionalized material.

Minor changes in the N 1s spectra after Pd adsorption suggest that N-containing groups may contribute secondarily to metal uptake. The most pronounced change was observed in the peak associated with amine groups (Fig. 7–C), likely originating from unreacted amine functionalities remaining after TA immobilization. Protonation of these groups under acidic conditions can result in electrostatic interaction with negatively charged Pd/Pt chloro-complexes, providing non-specific adsorption sites that may partly explain the minor co-adsorption of Pt. The C 1s and O 1s spectra also indicate changes in the organic surface environment after Pd uptake (Table S6). The increased contribution of carbonyl/amide-related carbon and the dominant O 1s component at 531.07 eV suggest perturbation of the amide/carboxylate environment after Pd binding, consistent with the sensitivity of C 1s/O 1s XPS signals to oxygenated organic groups and metal–carboxylate bonding, as well as the reported ability of Pd(II) to interact with amide carbonyl oxygen [73,74]. However, these changes should be interpreted as secondary effects, since the main mechanistic evidence arises from the redistribution of the S 2p components and the presence of Pd(II) together with chloride.

Taken together, these findings support a sulfur-assisted ligand-exchange mechanism for Pd uptake. This interpretation is consistent with molecular Pd(II)–disulfide studies in chloride media, which provide a mechanistic basis for the preferential interaction of Pd with TA-derived sulfur sites. In acidic chloride media, Pd(II) is mainly present as square-planar $[PdCl_4]^{2-}$, which can undergo associative chloride-to-sulfur substitution to yield species of the type $[PdCl_n(L–S)_m]$ depending on ligand denticity and geometry. This is supported by Pd(II)–disulfide model systems, where $[PdCl_4]^{2-}$ forms S-coordinated complexes through chloride displacement; for L-cystine, a monodentate Pd—S complex was reported with $\log K_1 \approx 3.3$, $\Delta H = -27$ kJ·mol^{-1}, and Ea = 66 ± 4 kJ·mol^{-1}, without detectable S—S bond fission under strongly

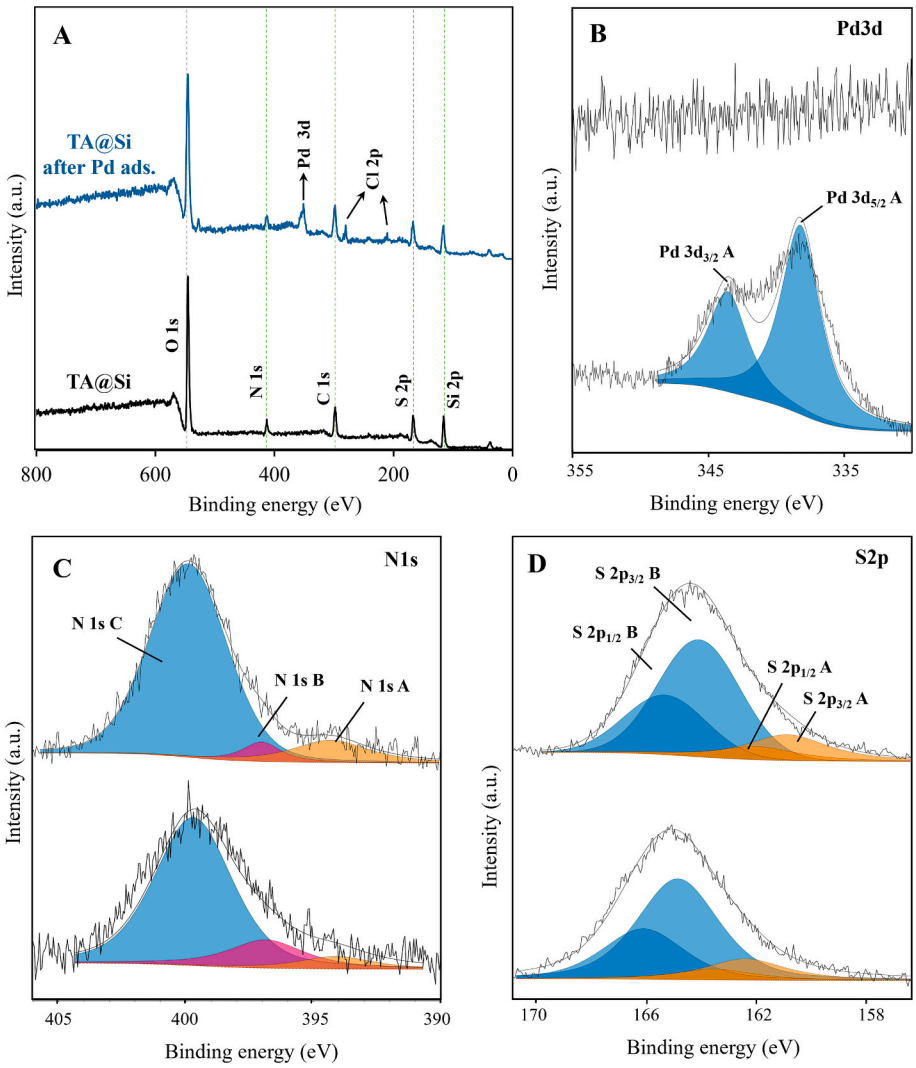

Fig. 7. **(A)** Wide–scan XPS survey spectra. High–resolution XPS spectra of **(B)** Pd 3d, **(C)** N 1s, and **(D)** S 2p regions. Each panel shows spectra of TA@Si before (top) and after Pd adsorption (bottom).

acidic conditions [72]. More generally, DFT calculations on several disulfides show that Pd(II) can stabilize S/S′-coordinated binuclear intermediates, with calculated log β values of 5.22–9.83 for representative S/S′-Pd disulfide complexes, depending on ligand structure and the density functional used [19]. In addition, computational studies indicate that Pt–disulfide interactions proceed through substantially greater S—S bond elongation, with calculated transition-state S—S distances of approximately 2.42–2.54 Å compared with 2.07–2.18 Å for Pd, indicating a significantly higher structural reorganization requirement for Pt coordination [21]. Pt is therefore less efficiently adsorbed because it is stabilized in the leaching medium mainly as the octahedral, substitution-inert complex. Thus, the preferential uptake of Pd does not arise from sulfur affinity alone, since Pt can also interact with sulfur donors, but from the greater ligand-exchange lability of $[PdCl_4]^{2-}$ and the lower structural reorganization required for Pd(II) coordination to TA-derived disulfide sulfur sites compared with the more chloride-stabilized and kinetically resistant Pt chloro complexes.

3.4. Desorption

Desorption experiments were conducted to identify and optimize an effective eluent for the separation of Pd and Pt adsorbed onto TA@Si. Different concentrations of HCl (1, 2, and 4 M), NaSCN (0.2, 0.5, and 1 M), and thiourea (TU) (0.2, 0.5, and 1 M in 0.5 M HCl) were evaluated (Fig. 8–A). All tested HCl solutions exhibited poor desorption performance for both metals. NaSCN solutions showed moderate desorption efficiencies, with a clear preference for Pd over Pt (Fig. 8–A). Pd desorption reached approximately 60% at both 0.5 and 1 M NaSCN, whereas Pt desorption remained limited to about 20–23%. This may be attributed to the greater ligand lability of Pd(II) chloro-complexes compared with the kinetically inert Pt(IV) chloro-complexes, rendering Pd—S bonds more susceptible to competitive ligand exchange and metal release into solution [9]. However, the highest desorption efficiencies were obtained using TU in 0.5 M HCl. Pd desorption approached 100% only at the highest TU concentration tested, whereas Pt desorption was nearly quantitative at all concentrations (Fig. 8–A). Consequently, 1 M TU in 0.5 M HCl was selected as the optimal desorption solution. The high desorption efficiency observed with thiourea indicates that Pd(II) remains accessible for ligand exchange, consistent with coordination to surface sulfur sites rather than irreversible binding.

To assess the operational stability and reusability of TA@Si, the material was subjected to five successive adsorption–desorption cycles and monitored for any loss of adsorption capacity during repeated use. In each cycle, adsorption was conducted using a fresh HCl–based multi–metallic solution, while desorption was performed with 1 M thiourea in 0.5 M HCl (Fig. 8–B). The results showed that the adsorption capacity of TA@Si remains stable over at least five cycles. Although a slight

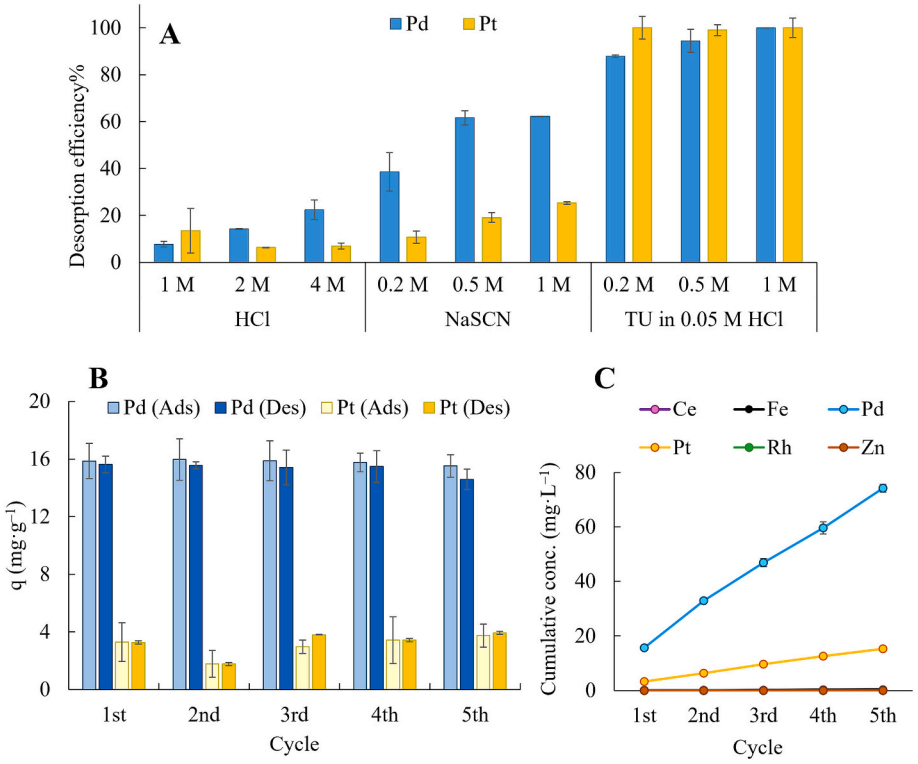

Fig. 8. **(A)** Desorption efficiency of Pd and Pt from TA@Si using different desorption agents and concentrations, for initial loadings of (15.87 ± 0.41) mg·g^{-1} Pd and (3.30 ± 0.05) mg·g^{-1} Pt. **(B)** Adsorbed and desorbed amounts of Pd and Pt (mg·g^{-1} of TA@Si) over successive adsorption–desorption cycles, with adsorption performed from a multi–metallic solution (20 ± 2) mg·L^{-1} of each metal in 0.2 M HCl and desorption using 1 M thiourea +0.5 M HCl. **(C)** Cumulative metals concentrations in the eluate over five cycles corresponding to Fig. 8–B.

decrease in desorption efficiency was observed when the same desorption solution was reused (Fig. 8–B), the concentrations of Pd and Pt in the eluate increased almost linearly with the number of cycles, reaching approximately (74.18 ± 1.41) mg·L^{-1} for Pd and (15.22 ± 0.11) mg·L^{-1} for Pt after five cycles (Fig. 8–C), while the concentrations of the other metals in the eluate remained negligible.

Compared to Trieu et al. [29], who reported a sharp drop in adsorption efficiency (down to ~20% by the 4th cycle) for carboxylate–linked TA on ZrO_2 due to hydrolytic instability, and only moderate improvement (~80% retention) with a phosphonate intermediate, TA@Si maintained stable Pd adsorption capacity over five cycles in 0.2 M HCl with excellent reusability. The robust silane–mediated covalent attachment (Si—C and amide bonds) provides superior acid stability, making TA@Si more suitable for practical hydrometallurgical applications.

The reversible adsorption–desorption behavior observed supports a mechanism in which Pd(II) interacts with a polarized disulfide motif through coordination, rather than undergoing complete reductive cleavage to form permanently bound thiolate species. While minor formation of thiolate–type species during adsorption cannot be

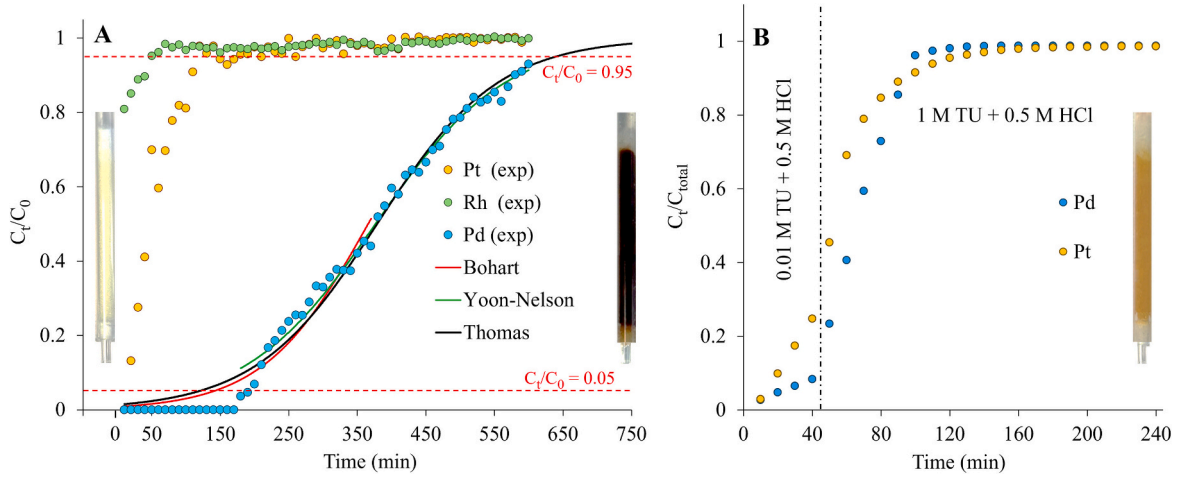

Fig. 9. **(A)** Breakthrough curves for PGMs adsorption onto TA@Si in a fixed–bed column, using a multi-metallic feed solution containing (50 ± 5) mg·L^{-1} of each metal in 0.2 M HCl; **(B)** desorption profiles obtained from the loaded column using two different eluents. Photographs of the column before (left), after adsorption (middle), and after desorption (right) illustrate changes in bed appearance. Experimental conditions: flow rate of 1 mL·min^{-1}, bed mass = 0.5435 g, bed radius = 0.25 and height = 4 cm (bed volume ≈ 0.785 cm^3), temperature at 303 K.

excluded, the absence of performance degradation over repeated cycles suggests that such processes do not dominate under the studied conditions.

3.5. Continuous–flow fixed–bed column evaluation

Breakthrough curve analysis is essential for the design and scale-up of fixed-bed adsorption systems for industrial applications. Accordingly, a preliminary fixed-bed column experiment was conducted (Fig. 9–A) to evaluate the practical applicability and dynamic selectivity of TA@Si under continuous–flow conditions. The experiment was performed at a flow rate (Q) of 1 mL·min^{-1}, using a multi–metal solution with individual metal concentrations of (50 ± 5) mg·L^{-1}. The column was packed with 0.5435 g of adsorbent, with a bed height of 4 cm and a radius of 0.25 cm (total volume of adsorbent of 0.785 cm^3).

The breakthrough curves for Pd, Pt, and Rh are presented in Fig. 9–A, with the remaining metals shown in Fig. S5. Pt and Rh exhibited rapid breakthrough, with C_t/C_0 rising sharply and approaching 1 within the first hour (Pt reached $C_t/C_0 \approx 0.17$ after 20 min, while Rh reached ≈ 0.8 after only 10 min). Consistent with the batch experiments, limited Pt and Rh uptake was observed, while no measurable removal of the remaining metals was detected. In contrast, Pd exhibited a markedly delayed breakthrough, with $C_t/C_0 = 0.05$ reached at 195 min (248 bed volumes), and exhaustion ($C_t/C_0 > 0.90$) occurring only after 580 min (Fig. 9–A). The extended plateau region reflects strong and selective adsorption of Pd during continuous operation. The dynamic adsorption capacity was determined by numerical integration of the breakthrough curve using the trapezoidal rule, according to the following equation, over the C_t/C_0 range of 0.05–0.90 (Q = 0.001 L·min^{-1}; m = 0.5435 g).

$$q_{dyn}\ (\mathrm{mg{\cdot}g^{-1}}) = \left(\frac{Q}{m} \times \int_0^t (C_0 - C_t)dt\right.$$

The dynamic capacity increased from 18.10 mg·g^{-1} at 5% breakthrough to 34.14 mg·g^{-1} at exhaustion. Moreover, bed utilization was quantified as the ratio of dynamic adsorption capacity to the equilibrium capacity obtained under batch conditions (q_{dyn}/q_{eq}), serving as a metric for adsorbent efficiency under continuous–flow operation [75]. The results indicate ~36.5% utilization at breakthrough and ~ 69% at exhaustion relative to the equilibrium capacity for Pd obtained under batch conditions.

Based on the batch isotherm results, which were well described by Langmuir–type models, the nonlinear form of the Thomas model [76] was applied to describe the Pd breakthrough behavior using the following equation:

$$\frac{C_t}{C_0} = \frac{1}{1 + \exp\left(\frac{k_{Th}}{Q}(q_{Th}m - C_0Qt)\right)}$$

The model parameters (k_{Th} and q_{Th}) were obtained by direct nonlinear least–squares fitting to the experimental breakthrough data.

The Thomas model provided an excellent fit to the experimental data (R^2 = 0.99), yielding a maximum adsorption capacity of 36.70 mg·g^{-1}, in good agreement with the experimental dynamic capacity (Fig. 9–A; Table S7). The relatively low Thomas rate constant ($k_{Th} = 2.15 \times 10^{-5}$ mL·mg^{-1}·min^{-1}) indicates that, under continuous–flow conditions, the overall adsorption rate is significantly influenced by mass transfer limitations. This observation agrees with the batch kinetic results, where the pseudo–second–order model showed that chemisorption (ligand exchange with TA's disulfide groups) is the intrinsic rate–limiting step in well–agitated systems. The apparent difference arises because intense mechanical stirring in batch experiments largely eliminates external film and intraparticle diffusion resistances, revealing the true surface reaction kinetics. In contrast, the fixed–bed column operates under much shorter residence times (~0.785 min), where external film diffusion, intraparticle diffusion, and axial dispersion become relevant and govern the overall breakthrough behavior.

To further analyze the initial region of the breakthrough curves, the Bohart–Adams model was applied, which describes the adsorption kinetics based on surface reaction theory and is particularly suitable for the early stage of column operation [77]. The model assumes that the adsorption rate is proportional to both the adsorbent residual capacity and the adsorbate concentration. The nonlinear form of the Bohart–Adams equation is expressed as equation below:

$$\frac{C_t}{C_0} = \exp\left(k_{BA}C_0t - k_{BA}N_0\frac{Z}{u}\right)$$

where k_{BA} is the Bohart–Adams kinetic constant (L·mg·min^{-1}), N_0 is the saturation concentration (mg·L^{-1}), Z is the bed height (cm), and u is the linear velocity (cm·min^{-1}).

The Bohart–Adams model was fitted to the initial region of the breakthrough curve (C_t/C_0 from 0.05 to 0.5), where the model's assumptions are valid. Data points beyond this region were excluded due to deviations from ideal plug flow behavior and increasing influence of axial dispersion. This model provided a moderate fit (R^2 = 0.88) to the initial breakthrough region ($0.05 \le C_t/C_0 \le 0.50$). The derived parameters ($k_{BA} = 3.19 \times 10^{-4}$ L·mg^{-1}·min^{-1} and $N_0 = 2.20 \times 10^4$ mg·L^{-1}) are consistent with the Thomas model and batch results, confirming high capacity and transport–limited behavior during early column operation (Table S7).

Furthermore, the breakthrough data were fitted using the nonlinear Yoon–Nelson model [78], expressed as:

$$\frac{C_t}{C_0} = \frac{1}{1 + \exp[k_{YN}(\tau - t)}$$

where t is time, k_{YN} is the Yoon–Nelson rate constant, and τ is the time for 50% breakthrough.

The Yoon–Nelson model provided an excellent fit to the experimental breakthrough data (R^2 = 0.99), indicating that the model adequately describes the dynamic adsorption behavior of Pd under the studied conditions. The rate constant (k_{YN} = 0.01 min^{-1}) is indicative of a gradual breakthrough profile, consistent with strong Pd–TA@Si interactions and possible mass transfer limitations within the column. The characteristic time parameter (τ = 376.38 min), corresponding to 50% breakthrough, further confirms the delayed saturation of the column and highlights the material's high affinity for Pd.

The mass transfer zone (MTZ) length was calculated from the breakthrough and exhaustion times using the following equation:

$$MTZ = L \times \frac{t_{0.90} - t_{0.05}}{t_{0.90}}$$

where L is the bed height, and $t_{0.05}$ and $t_{0.90}$ correspond to $C_t/C_0 = 0.05$ and 0.90, respectively. The value of $t_{0.90}$ was used as a practical approximation of exhaustion, as the breakthrough curve did not reach a higher conversion within the experimental timeframe (Table S7). For Pd, the MTZ length was estimated to be 2.42 cm, corresponding to approximately 61% of the total bed height. This relatively broad MTZ indicates that adsorption occurred over a substantial portion of the fixed bed, suggesting the influence of mass transfer limitations under the applied flow conditions.

After completion of the adsorption cycle and establishment of the breakthrough profile, desorption experiments were performed to evaluate metal recovery and assess the feasibility of stepwise Pd/Pt fractionation. The total metal loading on the column was 36.32 mg of Pd and 5.22 mg of Pt. A sequential elution strategy employing eluents of increasing complexation strength was applied: 0.01 M TU in 0.5 M HCl and 1 M TU in 0.5 M HCl (Fig. 9–B). Initial elution with 0.01 M TU in 0.5 M HCl for 40 min (≈51 bed volumes) resulted in the co-elution of both Pd and Pt, with a slightly higher normalized release of Pt (expressed as C_t/C_{total}). During this stage, 3.02 mg of Pd and 1.26 mg of Pt were recovered, leading to partial enrichment of Pd on the adsorbent. A

pronounced increase in desorption was observed upon introduction of 1 M TU in 0.5 M HCl (from 50 min onward), where strong ligand exchange facilitated rapid metal release. The normalized concentration (C_t/C_{total}) reached >0.97 for Pd at 100 min, while Pt reached 0.93. Within the 50–100 min interval, approximately 91% of the total Pd was recovered, and the Pd fraction in the eluate reached ~94%, demonstrating the potential of fractionated elution to enhance Pd purity in the recovered stream. No detectable levels of other metals, including Rh, were observed in the eluate fractions.

From a process perspective, the sustained Pd selectivity, extended breakthrough behavior, and effective fractionated desorption demonstrate that TA@Si is well–suited for continuous fixed–bed operation, enabling selective Pd recovery from complex chloride leachates prior to downstream refining [75, 79]. The high number of treated bed volumes and the stable performance under strongly acidic conditions further support its potential integration into industrial hydrometallurgical circuits, where efficiency, selectivity, and reliable column operation are critical design criteria.

3.6. Scalability, cost considerations, and solvent management

The grafting protocol used in this work, involving amino-silanization of the silica surface followed by DCC/NHS-mediated coupling of TA, is a mature and widely adopted bioconjugation strategy, contributing to the reproducibility and reliability of the resulting surface functionalization. However, from a preliminary economic perspective, the current synthesis should therefore be considered a proof-of-concept route rather than an optimized preparation method. The main advantage of the protocol is that the support and key reagents, including silica gel, APTMS, and TA, are commercially available, and the resulting silane/amide anchoring provides the acid stability required for repeated operation in chloride-rich media. Nevertheless, the present laboratory protocol uses excess APTMS, TA, DCC, and NHS relative to the final sulfur loading of the adsorbent. In addition, the DCC/NHS step generates stoichiometric dicyclohexylurea (DCU) as a by-product, whose removal at larger scale can complicate purification [80].

Furthermore, the current synthesis relies on dry organic solvents (toluene for silanization and DCM/acetonitrile for TA activation and coupling) generating substantial solvent waste. At larger scale, solvent recovery and reuse will be essential to improve economics and reduce environmental impact. In the silanization step, optimization should focus on lowering the APTMS/toluene ratio, recovering toluene after filtration, and evaluating vapor-phase aminosilane deposition as a lower-solvent alternative [81]. For TA activation and coupling, reducing DCM/acetonitrile volumes, recovering reusable fractions, and screening water-compatible carbodiimide or aqueous–alcoholic media (where compatible with TA solubility) would decrease chlorinated solvent use and simplify by-product handling [82]. Washing streams should be segregated by composition to enable recovery of DCM, ethanol, and methanol fractions, with dedicated treatment reserved for streams containing DCU or residual coupling reagents. While distillation remains the standard recovery approach, organic solvent nanofiltration and pervaporation may offer more energy-efficient options for selected dehydration or purification steps [83,84].

Finally, adsorbent durability and reusability are critical for practical implementation and economic viability, particularly under the strongly acidic hydrometallurgical conditions. The covalent immobilization of TA through silane and amide linkages conferred high chemical stability on TA@Si, enabling the adsorbent to maintain its performance over at least five adsorption–desorption cycles in acidic chloride media without observable loss of adsorption capacity. This repeated-use capability is important from an economic perspective, since the initial material preparation and associated capital costs can be amortized over multiple operating cycles rather than assigned to a single adsorption run. Moreover, the economics of Pd recovery are favored by the high intrinsic value of Pd and by the low operational intensity of the separation step, which is performed under mild conditions and mainly requires solution pumping/contacting and regeneration, without external heating or energy-intensive phase-change operations. Furthermore, the favorable breakthrough behavior and efficient regeneration observed under fixed-bed operation demonstrate that the material retains its functionality under dynamic flow conditions. Consequently, these characteristics position TA@Si as a promising candidate for integration into chloride-based Pd recovery flowsheets, provided that the grafting chemistry is further optimized for reagent economy and solvent management.

4. Conclusions

This study demonstrates that thioctic acid–functionalized mesoporous silica (TA@Si) is an effective and robust adsorbent for the selective recovery of Pd(II) from chloride–rich multi–metal systems. The material exhibits high selectivity over Pt, Rh, and base metals across a wide acidity range, while maintaining rapid adsorption kinetics and stable performance during repeated adsorption–desorption cycles. Spectroscopic analyses indicate that Pd(II) adsorption proceeds via coordination to disulfide sulfur atoms, forming mixed Pd–S/Cl complexes with no evidence for extensive S—S bond cleavage. Continuous–flow column experiments further confirm that this selectivity is preserved under dynamic conditions, with delayed Pd breakthrough and high bed utilization, demonstrating the practical applicability of the material. Efficient Pd recovery using thiourea solutions highlights the reversible nature of the adsorption process in both batch and continuous systems.

This work introduces an acid–stable thioctic–acid–functionalized silica adsorbent for selective Pd recovery from complex chloride–rich PGMs leachate simulants, demonstrating the combined advantages of disulfide–based coordination chemistry, broad HCl tolerance, multi–metal selectivity, regenerability, and continuous–flow compatibility. These results highlight the potential of disulfide–functionalized materials as selective, process–relevant alternatives to conventional sulfur–based adsorbents in hydrometallurgical applications.

CRediT authorship contribution statement

Amir Nobahar: Writing – original draft, Visualization, Investigation, Formal analysis, Data curation, Conceptualization. **Flavia N. Braga:** Writing – review & editing, Formal analysis. **Rita M. Carvalho:** Writing – review & editing, Formal analysis. **Helena Passos:** Writing – review & editing, Validation, Funding acquisition. **Filipe H.B. Sosa:** Writing – review & editing, Funding acquisition. **Nicolas Schaeffer:** Writing – review & editing, Validation, Methodology, Conceptualization. **João A. P. Coutinho:** Writing – review & editing, Supervision, Resources, Project administration, Conceptualization.

Declaration of competing interest

The authors declare that they have no known competing financial interests or personal relationships that could have appeared to influence the work reported in this paper.

Acknowledgements

This work was financially supported by national funds through FCT – Fundação para a Ciência e a Tecnologia, I.P., within the scope of the project PlatILPlus (2022.04478.PTDC, DOI: 10.54499/2022.04478.PTDC). This work was further financially supported by: LSRE–LCM, UID/50020/2025; ALiCE, LA/P/0045/2020 (DOI: 10.54499/LA/P/0045/2020); and CICECO–Aveiro Institute of Materials, UID/50011/2025 (DOI 10.54499/UID/50011/2025) & LA/P/0006/2020 (DOI 10.54499/LA/P/0006/2020), financed by national funds through the FCT/MCTES (PIDDAC). N. Schaeffer acknowledges the European Union for the European Research Council (ERC) for the starting grant DESignSX (Grant agreement ID: 101116461) (doi:https://doi.org/10.3030/

101116461). F.H.B. Sosa, F. Braga and R. Carvalho acknowledge FCT for the researcher contract CEECIND/07209/2022 (10.54499/2022.07209.CEECIND/CP1720/CT0019) and the Ph.D. grants 2023.01749.BD (DOI:10.54499/2023.01749.BD) and 2025.06718.BDANA, respectively. The NMR spectrometers are part of the National NMR Network (PTNMR) and are partially supported by Infrastructure Project N° 022161 (co–financed by FEDER through COMPETE 2020, POCI and PORL and FCT through PIDDAC).

Appendix A. Supplementary data

Supplementary data to this article can be found online at https://doi.org/10.1016/j.cej.2026.178604.

Data availability

Data will be made available on request.

References

[1] D. Xun, H. Hao, X. Sun, Z. Liu, F. Zhao, End-of-life recycling rates of platinum group metals in the automotive industry: insight into regional disparities, J. Clean. Prod. 266 (2020) 121942, https://doi.org/10.1016/j.jclepro.2020.121942.
[2] Thunder Said Energy, Going platinum: PGMs in energy transition?, in: Thunder Said Energy, 2024. https://thundersaidenergy.com/2024/09/19/going-platinum-pgms-in-energy-transition/. (Accessed 18 June 2026).
[3] U.S. Geological Survey, Platinum-group metals, in: 2021 Minerals Yearbook, U.S. Department of the Interior, U.S. Geological Survey, Reston, VA, 2025. https://pubs.usgs.gov/myb/vol1/2021/myb1-2021-platinum-group.pdf.
[4] S. Kang, T. Ouchi, T.H. Okabe, Novel concentration process for platinum group metals in automotive exhaust catalyst using electroless copper plating, sulfurization, and flotation, Metall. Mater. Trans. B Process Metall. Mater. Process. Sci. 55 (2024) 32–52, https://doi.org/10.1007/s11663-023-02880-8.
[5] J. Qiao, X. Guo, D. Li, M. Li, Optimized recovery of platinum group metals (PGMs) from spent automotive catalysts via industrial steelmaking slag utilization, Adv. Sustainable Syst. 9 (2025) e00195, https://doi.org/10.1002/adsu.202500195.
[6] S. Kolbadinejad, A. Ghaemi, Recovery and extraction of platinum from spent catalysts: a review, Case Stud. Chem. Environ. Eng. 7 (2023) 100327, https://doi.org/10.1016/j.cscee.2023.100327.
[7] I. Yakoumis, A.M. Moschovi, I. Giannopoulou, D. Panias, Real life experimental determination of platinum group metals content in automotive catalytic converters, IOP Conf. Ser.: Mater. Sci. Eng. 329 (2018) 012009, https://doi.org/10.1088/1757-899X/329/1/012009.
[8] B. Xu, Y. Chen, Y. Zhou, B. Zhang, G. Liu, Q. Li, Y. Yang, T. Jiang, A review of recovery of palladium from the spent automobile catalysts, Metals 12 (2022) 533, https://doi.org/10.3390/met12040533.
[9] F.L. Bernardis, R.A. Grant, D.C. Sherrington, A review of methods of separation of the platinum-group metals through their chloro-complexes, React. Funct. Polym. 65 (2005) 205–217, https://doi.org/10.1016/j.reactfunctpolym.2005.05.011.
[10] M.K. Jha, D. Gupta, J. Lee, V. Kumar, J. Jeong, Solvent extraction of platinum using amine based extractants in different solutions: a review, Hydrometallurgy 142 (2014) 60–69, https://doi.org/10.1016/j.hydromet.2013.11.009.
[11] H. Narita, R. Kasuya, T. Suzuki, R. Motokawa, M. Tanaka, Precious metal separations, in: R.A. Scott (Ed.), Encyclopedia of Inorganic and Bioinorganic Chemistry, 2nd ed., Wiley, 2020, pp. 1–28, https://doi.org/10.1002/9781119951438.eibc2756.
[12] D. Nagai, Y. Nonaka, T. Akiyama, R. Takahashi, T. Yamanobe, Mutual separation of platinum group metals via seed-mediated growth on a polymer with metal-coordination unit, Sep. Purif. Technol. 276 (2021) 119265, https://doi.org/10.1016/j.seppur.2021.119265.
[13] A. Paul, A.S. Suneesh, N. Ramanathan, A sulfur-based adsorbent for the removal of palladium from aqueous waste: comprehensive study on the preparation, characterization, adsorption and breakthrough modeling, Colloids Surf. A Physicochem. Eng. Asp. 714 (2025) 136577, https://doi.org/10.1016/j.colsurfa.2025.136577.
[14] T. Kang, Y. Park, J. Yi, Highly selective adsorption of Pt^{2+} and Pd^{2+} using thiol-functionalized mesoporous silica, Ind. Eng. Chem. Res. 43 (2004) 1478–1484, https://doi.org/10.1021/ie030590k.
[15] L. Zhou, J. Liu, Z. Liu, Adsorption of platinum(IV) and palladium(II) from aqueous solution by thiourea-modified chitosan microspheres, J. Hazard. Mater. 172 (2009) 439–446, https://doi.org/10.1016/j.jhazmat.2009.07.030.
[16] M.R.R. Mphahlele, A.K. Mosai, H. Tutu, I.A. Kotzé, Efficient recovery of platinum and palladium by fixed-bed column adsorption using acylthiourea- and amine-modified silica, J. Sustain. Metall. 11 (2025) 4334–4346, https://doi.org/10.1007/s40831-025-01253-6.
[17] A.I. Petrov, Interaction of disulfides with metal ions and spectroscopic identification of the products, Coord. Chem. Rev. 505 (2024) 215678, https://doi.org/10.1016/j.ccr.2024.215678.
[18] A. Nobahar, H. Passos, N. Schaeffer, F.H.B. Sosa, J.A.P. Coutinho, Engineered biopolymer architectures for selective metal ions extraction, Adv. Sustainable Syst. 10 (2026) e70457, https://doi.org/10.1002/adsu.70457.
[19] A.I. Petrov, V.D. Dergachev, Palladium(II) ion mediated disulfide/thiolate interconversion: predicting the disulfide group state from first principles, J. Phys. Chem. A 123 (2019) 4873–4882, https://doi.org/10.1021/acs.jpca.9b00740.
[20] A.I. Petrov, M.A. Lutoshkin, TD-DFT assessment of UV-vis spectra palladium and platinum complexes with thiols and disulfides, J. Mol. Model. 27 (2021) 152, https://doi.org/10.1007/s00894-021-04781-6.
[21] A.I. Petrov, Experimental and DFT study of the kinetics of the interaction of Pt(II) and Pd(II) with disulfides in hydrochloric acid solutions, Inorg. Chim. Acta 545 (2023) 121269, https://doi.org/10.1016/j.ica.2022.121269.
[22] A.I. Petrov, I.D. Dergachev, Platinum(II)-mediated disulfide/thiolate interconversion in organic disulfides: density functional theory thermodynamic study, Int. J. Quantum Chem. 122 (2022) e26849, https://doi.org/10.1002/qua.26849.
[23] N. Wada, H. Wakami, T. Konishi, S. Matsugo, The degradation and regeneration of α-lipoic acid under the irradiation of UV light in the existence of homocysteine, J. Clin. Biochem. Nutr. 44 (2009) 218–222, https://doi.org/10.3164/jcbn.08-215.
[24] J. Wang, Z. Chu, S. Zheng, Exploring α-lipoic acid based thermoplastic silicone adhesive: towards sustainable and green recycling, Polymers 16 (2024) 3254, https://doi.org/10.3390/polym16233254.
[25] I. Turcu, I. Zarafu, M. Popa, M. Chifiriuc, C. Bleotu, D. Culita, C. Ghica, P. Ionita, Lipoic acid gold nanoparticles functionalized with organic compounds as bioactive materials, Nanomaterials 7 (2017) 43, https://doi.org/10.3390/nano7020043.
[26] A. Narani, H.P. Reddy Kannapu, K. Natte, D.R. Burri, Pd-nanoparticles immobilized organo-functionalized SBA-15: an efficient heterogeneous catalyst for selective hydrogenation of C=C double bonds of α,β-unsaturated carbonyl compounds, Mol. Catal. 497 (2020) 111200, https://doi.org/10.1016/j.mcat.2020.111200.
[27] G. Liu, R. Yu, J. Jiang, Z. Ding, J. Ma, R. Liang, Robust immobilization of anionic silver nanoparticles on cellulose filter paper toward a low-cost point-of-use water disinfection system with improved anti-biofouling properties, RSC Adv. 11 (2021) 4873–4882, https://doi.org/10.1039/D0RA09152A.
[28] M.A.E. Hassan, W.A. Khalil, S.A. Abdelnour, R.M. Aman, Supplementation of alpha-lipoic acid-loaded nanoliposomes in semen extender improves freezability of buffalo spermatozoa, Sci. Rep. 12 (2022) 22464, https://doi.org/10.1038/s41598-022-26960-y.
[29] Q.A. Trieu, S. Pellet-Rostaing, G. Arrachart, Y. Traore, S. Kimbel, S. Daniele, Interfacial study of surface-modified ZrO2 nanoparticles with thioctic acid for the selective recovery of palladium and gold from electronic industrial wastewater, Sep. Purif. Technol. 237 (2020) 116353, https://doi.org/10.1016/j.seppur.2019.116353.
[30] N. Gys, B. Pawlak, L.L. Lufungula, K. Marcoen, K. Wyns, K. Baert, T.A. Atia, J. Spooren, P. Adriaensens, F. Blockhuys, T. Hauffman, V. Meynen, S. Mullens, B. Michielsen, Selective Pd recovery from acidic leachates by 3-mercaptopropyl-phosphonic acid grafted TiO_2: does surface coverage correlate to performance? RSC Adv. 12 (2022) 36046–36062, https://doi.org/10.1039/D2RA07214A.
[31] N. Anand, P. Ramudu, K.H.P. Reddy, K.S.R. Rao, B. Jagadeesh, V.S.P. Babu, D. R. Burri, Gold nanoparticles immobilized on lipoic acid functionalized SBA-15: synthesis, characterization and catalytic applications, Appl. Catal. A Gen. 454 (2013) 119–126, https://doi.org/10.1016/j.apcata.2013.01.006.
[32] N.F. Abd Razak, M. Shamsuddin, S.L. Lee, Adsorption kinetics and thermodynamics studies of gold(III) ions using thioctic acid functionalized silica coated magnetite nanoparticles, Chem. Eng. Res. Des. 130 (2018) 18–28, https://doi.org/10.1016/j.cherd.2017.12.004.
[33] B. Jarrais, C. Pereira, A.R. Silva, A.P. Carvalho, J. Pires, C. Freire, Grafting of vanadyl acetylacetonate onto organo-hexagonal mesoporous silica and catalytic activity in the allylic epoxidation of geraniol, Polyhedron 28 (2009) 994–1000, https://doi.org/10.1016/j.poly.2008.12.049.
[34] Z. Wang, G. Dan, R. Zhang, L. Ma, K. Lin, Coupling and decoupling CH stretching vibration of methylene and methine in serine conformers, Spectrochim. Acta A Mol. Biomol. Spectrosc. 285 (2023) 121829, https://doi.org/10.1016/j.saa.2022.121829.
[35] N. Ikuta, T. Endo, S. Hosomi, K. Setou, S. Tanaka, N. Ogawa, H. Yamamoto, T. Mizukami, S. Arai, M. Okuno, K. Takahashi, K. Terao, S. Matsugo, Structural analysis of crystalline R(+)-α-lipoic acid-α-cyclodextrin complex based on microscopic and spectroscopic studies, Int. J. Mol. Sci. 16 (2015) 24614–24628, https://doi.org/10.3390/ijms161024614.
[36] M. Gühlke, Z. Heiner, J. Kneipp, Surface-enhanced Raman and surface-enhanced hyper-Raman scattering of thiol-functionalized carotene, J. Phys. Chem. C 120 (2016) 20702–20709, https://doi.org/10.1021/acs.jpcc.6b01895.
[37] A.S. Maria Chong, X.S. Zhao, Functionalization of SBA-15 with APTES and characterization of functionalized materials, J. Phys. Chem. B 107 (2003) 12650–12657, https://doi.org/10.1021/jp035877.
[38] J.V. Paukstelis, E.F. Byrne, T.P. O'Connor, T.E. Roche, Carbon-13 nuclear magnetic resonance spectra of thiols and thiolacetates: lipoic acid and derivatives, J. Organomet. Chem. 42 (1977) 3941–3944, https://doi.org/10.1021/jo00444a033.
[39] M.J. Duer (Ed.), Solid-State NMR Spectroscopy Principles and Applications, 1st ed., Wiley, 2001 https://doi.org/10.1002/9780470999394.
[40] K.S.W. Sing, Reporting physisorption data for gas/solid systems with special reference to the determination of surface area and porosity (recommendations 1984), Pure Appl. Chem. 57 (1985) 603–619, https://doi.org/10.1351/pac198557040603.
[41] M. Thommes, K. Kaneko, A.V. Neimark, J.P. Olivier, F. Rodriguez-Reinoso, J. Rouquerol, K.S.W. Sing, Physisorption of gases, with special reference to the

evaluation of surface area and pore size distribution (IUPAC technical report), Pure Appl. Chem. 87 (2015) 1051–1069, https://doi.org/10.1515/pac-2014-1117.
[42] M.H. Lim, A. Stein, Comparative studies of grafting and direct syntheses of inorganic−organic hybrid mesoporous materials, Chem. Mater. 11 (1999) 3285–3295, https://doi.org/10.1021/cm990369r.
[43] M. Hosseinzadeh, J. Petersen, Platinum(IV), palladium(II), and rhodium(III) recovery from mixed acidic chloride solutions using chelating ion exchange resin Puromet MTS9600, Solvent Extr. Ion Exch. 42 (2024) 609–635, https://doi.org/10.1080/07366299.2024.2446472.
[44] Y.S. Ho, G. McKay, Pseudo-second order model for sorption processes, Process Biochem. 34 (1999) 451–465, https://doi.org/10.1016/S0032-9592(98)00112-5.
[45] J. Febrianto, A.N. Kosasih, J. Sunarso, Y.-H. Ju, N. Indraswati, S. Ismadji, Equilibrium and kinetic studies in adsorption of heavy metals using biosorbent: a summary of recent studies, J. Hazard. Mater. 162 (2009) 616–645, https://doi.org/10.1016/j.jhazmat.2008.06.042.
[46] O.P. Murphy, M. Vashishtha, P. Palanisamy, K.V. Kumar, A review on the adsorption isotherms and design calculations for the optimization of adsorbent mass and contact time, ACS Omega 8 (2023) 17407–17430, https://doi.org/10.1021/acsomega.2c08155.
[47] S. Kalam, S.A. Abu-Khamsin, M.S. Kamal, S. Patil, Surfactant adsorption isotherms: a review, ACS Omega 6 (2021) 32342–32348, https://doi.org/10.1021/acsomega.1c04661.
[48] D. Zhang, L. MacDonald, P. Raj, A.K. Karamalidis, Thiol-functionalized cellulose adsorbents for highly selective separation of palladium over platinum in acidic aqueous solutions, Chem. Eng. J. 494 (2024) 152948, https://doi.org/10.1016/j.cej.2024.152948.
[49] A. Nobahar, F.N. Braga, F.H.B. Sosa, N. Schaeffer, J.A.P. Coutinho, H. Passos, Waste–to–waste valorization: sustainable palladium recovery from real spent catalytic converter leachates using chicken feathers, Waste Manag. 212 (2026) 115349, https://doi.org/10.1016/j.wasman.2026.115349.
[50] Z. Ye, H. Zhang, X. Chen, L. Chen, K. Thummavichai, X. Wang, T. Fujita, Y. Wei, Silica-supported thiourea resin for efficient recovery of Pd(II): batch, column and mechanism study, J. Clean. Prod. 423 (2023) 138684, https://doi.org/10.1016/j.jclepro.2023.138684.
[51] M.M. Mahleba, J.-L. Mukaba, Z.R. Tshentu, Selective recovery of palladium (II) from acidic solutions using dithio- and benzimidazolylthio-functionalized resins, Minerals 15 (2025) 589, https://doi.org/10.3390/min15060589.
[52] P. Moleko-Boyce, H. Makelane, M.Z. Ngayeka, Z.R. Tshentu, Recovery of platinum group metals from leach solutions of spent catalytic converters using custom-made resins, Minerals 12 (2022) 361, https://doi.org/10.3390/min12030361.
[53] V.N. Losev, E.V. Borodina, O.V. Buyko, A.S. Samoilo, E. Elsuf'ev, M. Li, Highly selective adsorbents based on silica gel chemically modified with sulfur-containing groups of arched structure for preconcentration and determination of palladium(II) in products of processing of sulfide copper-nickel ore, Microchem. J. 195 (2023) 109452, https://doi.org/10.1016/j.microc.2023.109452.
[54] J. Dobrzyńska, R. Dobrowolski, R. Olchowski, E. Zięba, M. Barczak, Palladium adsorption and preconcentration onto thiol- and amine-functionalized mesoporous silicas with respect to analytical applications, Microporous Mesoporous Mater. 274 (2019) 127–137, https://doi.org/10.1016/j.micromeso.2018.07.038.
[55] T. Ye, X. Zhang, W. Xu, H. Li, K. Tang, Nitrogen-rich sulfur-containing heterocyclic adsorbents for effective selective adsorption of au(III)/Pd(II)/Pt(IV), Chem. Eng. J. 498 (2024) 155695, https://doi.org/10.1016/j.cej.2024.155695.
[56] P.R. Zalupski, R. McDowell, G. Dutech, The adsorption of gold, palladium, and platinum from acidic chloride solutions on mesoporous carbons, Solvent Extr. Ion Exch. 32 (2014) 737–748, https://doi.org/10.1080/07366299.2014.951278.
[57] R.E.C. Torrejos, E.C. Escobar, J.W. Han, S.H. Min, H. Yook, K.J. Parohinog, S. Koo, H. Kim, G.M. Nisola, W.-J. Chung, Multidentate thia-crown ethers as hyper-crosslinked macroporous adsorbent resins for the efficient Pd/Pt recovery and separation from highly acidic spent automotive catalyst leachate, Chem. Eng. J. 424 (2021) 130379, https://doi.org/10.1016/j.cej.2021.130379.
[58] A. Muşină, V. Bocokić, V. Lavric, S. Van Zutphen, Phosphorus-based polymers for selective capture of platinum group metals, Ind. Eng. Chem. Res. 53 (2014) 13362–13369, https://doi.org/10.1021/ie502153f.
[59] M.N. Sahmoune, Evaluation of thermodynamic parameters for adsorption of heavy metals by green adsorbents, Environ. Chem. Lett. 17 (2019) 697–704, https://doi.org/10.1007/s10311-018-00819-z.
[60] T. Öztürk, M. Gülfen, A. Özdemir, Sorption of Pt(IV) ions on poly(m-aminobenzoic acid) chelating polymer: equilibrium, kinetic and thermodynamic studies, SN Appl. Sci. 2 (2020) 1886, https://doi.org/10.1007/s42452-020-03692-0.
[61] R. Gamal, S.E. Rizk, N.E. El-Hefny, Sorption of palladium(II) from aqueous solution using diphenylthiocarbazone immobilized onto kieselguhr, J. Inorg. Organomet. Polym. 32 (2022) 2455–2472, https://doi.org/10.1007/s10904-022-02365-2.
[62] R.J.H. Clark, M. Kurmoo, D.N. Mountney, H. Toftlund, Electronic and resonance Raman spectra of mixed-valence, linear-chain complexes of platinum and palladium with 1,2-diaminocycloalkanes, J. Chem. Soc. Dalton Trans. (1982) 1851–1860, https://doi.org/10.1039/DT9820001851.
[63] K. Nakamoto, Infrared and Raman spectra of inorganic and coordination compounds, 6th ed, Wiley, Hoboken, N.J, 2009, https://doi.org/10.1002/9780470405840.
[64] C.K.A. Nyamekye, S.C. Weibel, E.A. Smith, Directional Raman scattering spectra of metal–sulfur bonds at smooth gold and silver substrates, J. Raman Spectrosc. 52 (2021) 1246–1255, https://doi.org/10.1002/jrs.6124.
[65] T.S. Rufael, R.J. Koestner, E.B. Kollin, M. Salmeron, J.L. Gland, Adsorption and thermal decomposition of CH3SH on the Pt(111) surface, Surf. Sci. 297 (1993) 272–285, https://doi.org/10.1016/0039-6028(93)90216-7.
[66] W. Huang, C. Li, J. Wang, L. Zhu, Vibrational spectra and normal coordinate analysis for (*S*-glutathionato) (2,2′:6′,2′-terpyridine) platinum(II) chloride, [Pt (Trpy)Gs]cl, Spectrosc. Lett. 31 (1998) 1793–1809, https://doi.org/10.1080/00387019808007455.
[67] N. Bélanger-Desmarais, M. Schütz, C. Reber, Remarkably intricate Raman spectra of platinum(II)–ligand skeletal modes in diamminedihalido complexes, J. Phys. Chem. A 123 (2019) 5574–5579, https://doi.org/10.1021/acs.jpca.9b03893.
[68] N. Ikuta, A. Tanaka, A. Otsubo, N. Ogawa, H. Yamamoto, T. Mizukami, S. Arai, M. Okuno, K. Terao, S. Matsugo, Spectroscopic studies of R(+)-α-lipoic acid—cyclodextrin complexes, Int. J. Mol. Sci. 15 (2014) 20469–20485, https://doi.org/10.3390/ijms151120469.
[69] S. Moosun, S.J. Laulloo, M.G. Bhowon, Metal complexes of diaryl and 2,2′-dipyridyl disulfides, J. Sulfur Chem. 33 (2012) 661–691, https://doi.org/10.1080/17415993.2012.719897.
[70] D.G. Castner, K. Hinds, D.W. Grainger, X-ray photoelectron spectroscopy sulfur 2p study of organic thiol and disulfide binding interactions with gold surfaces, Langmuir 12 (1996) 5083–5086, https://doi.org/10.1021/la960465w.
[71] D. Mishra, S. Wang, S. Michel, G. Palui, N. Zhan, W. Perng, Z. Jin, H. Mattoussi, Photochemical transformation of lipoic acid-based ligands: probing the effects of solvent, ligand structure, oxygen and pH, Phys. Chem. Chem. Phys. 20 (2018) 3895–3902, https://doi.org/10.1039/C7CP06350D.
[72] A.I. Petrov, N.N. Golovnev, A.A. Leshok, A thermodynamic and kinetic study on $[PdCl_4]^{2-}$ complex formation with L-cystine, J. Coord. Chem. 65 (2012) 1339–1353, https://doi.org/10.1080/00958972.2012.672733.
[73] G.P. López, D.G. Castner, B.D. Ratner, XPS O 1s binding energies for polymers containing hydroxyl, ether, ketone and ester groups, Surf. Interface Anal. 17 (1991) 267–272, https://doi.org/10.1002/sia.740170508.
[74] O. Pérez, O.F. Odio, E. Reguera, XPS as a probe for the bonding nature in metal acetates, New J. Chem. 46 (2022) 11255–11265, https://doi.org/10.1039/D2NJ01905A.
[75] H. Patel, Fixed-bed column adsorption study: a comprehensive review, Appl Water Sci 9 (2019) 45, https://doi.org/10.1007/s13201-019-0927-7.
[76] H.C. Thomas, Heterogeneous ion exchange in a flowing system, J. Am. Chem. Soc. 66 (1944) 1664–1666, https://doi.org/10.1021/ja01238a017.
[77] G.S. Bohart, E.Q. Adams, Some aspects of the behavior of charcoal with respect to chlorine, J. Am. Chem. Soc. 42 (1920) 523–544, https://doi.org/10.1021/ja01448a018.
[78] Y.H. Yoon, J.H. Nelson, Application of gas adsorption kinetics I: a theoretical model for respirator cartridge service life, Am. Ind. Hyg. Assoc. J. 45 (1984) 509–516, https://doi.org/10.1080/15298668491400197.
[79] C. Vancea, M. Mihailescu, A. Negrea, G. Mosoarca, M. Ciopec, N. Duteanu, P. Negrea, V. Minzatu, Batch and fixed-bed column studies on palladium recovery from acidic solution by modified $MgSiO_3$, Int. J. Environ. Res. Public Health 17 (2020) 9500, https://doi.org/10.3390/ijerph17249500.
[80] E. Valeur, M. Bradley, Amide bond formation: beyond the myth of coupling reagents, Chem. Soc. Rev. 38 (2009) 606–631, https://doi.org/10.1039/B701677H.
[81] M. Sypabekova, A. Hagemann, D. Rho, S. Kim, Review: 3-aminopropyltriethoxysilane (APTES) deposition methods on oxide surfaces in solution and vapor phases for biosensing applications, Biosensors 13 (2022) 36, https://doi.org/10.3390/bios13010036.
[82] M. Badland, R. Crook, B. Delayre, S.J. Fussell, I. Gladwell, M. Hawksworth, R. M. Howard, R. Walton, G.A. Weisenburger, A comparative study of amide-bond forming reagents in aqueous media – substrate scope and reagent compatibility, Tetrahedron Lett. 58 (2017) 4391–4394, https://doi.org/10.1016/j.tetlet.2017.10.014.
[83] J.D. Chea, A.L. Lehr, J.P. Stengel, M.J. Savelski, C.S. Slater, K.M. Yenkie, Evaluation of solvent recovery options for economic feasibility through a superstructure-based optimization framework, Ind. Eng. Chem. Res. 59 (2020) 5931–5944, https://doi.org/10.1021/acs.iecr.9b06725.
[84] E.M. Rundquist, C.J. Pink, A.G. Livingston, Organic solvent nanofiltration: a potential alternative to distillation for solvent recovery from crystallisation mother liquors, Green Chem. 14 (2012) 2197, https://doi.org/10.1039/c2gc35216h.